Application of quantum-limited optical time transfer to space-based optical clock comparisons and coherent networks

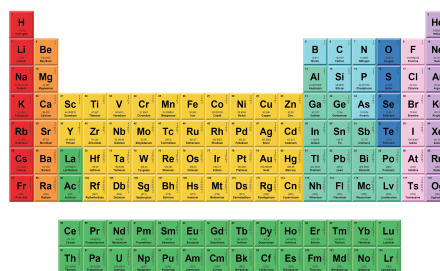Emily D. Caldwell ✉ ; Laura C. Sinclair ✉ ; Jean-Daniel Deschenes ; Fabrizio Giorgetta ; Nathan R. Newbury

Check for updates

CHORUS

View Online

Export Citation

APL Photonics

Application of quantum-limited optical time transfer to space-based optical clock comparisons and coherent networks (EP)

View Online   Export Citation   CrossMark

Emily D. Caldwell,[1,a] (iD) Laura C. Sinclair,[1,a] (iD) Jean-Daniel Deschenes,[2] (iD) Fabrizio Giorgetta[1,3] (iD)
and Nathan R. Newbury[1] (iD)

AFFILIATIONS

[1] National Institute of Standards and Technology, 325 Broadway, Boulder, Colorado 80305, USA
[2] Octosig Consulting, Quebec City, Quebec G2K 1X6, Canada
[3] Department of Physics, University of Colorado, Boulder, Colorado 80305, USA

Note: This paper is part of the APL Photonics Special Topic on State-of-the-Art and Future Directions in Optical Frequency Comb Sources, Enabling Technologies, and Applications.
[a] Authors to whom correspondence should be addressed: emily.caldwell@nist.gov and laura.sinclair@nist.gov

ABSTRACT

With the demonstration of quantum-limited optical time transfer capable of tolerating the losses associated with long ground-to-space links, two future applications of free-space time transfer have emerged: intercontinental clock comparisons for time dissemination and coherence transfer for future distributed sensing in the mm-wave region. In this paper, we estimated the projected performance of these two applications using quantum-limited optical time transfer and assuming existing low-size, low-weight, and low-power hardware. In both cases, we limit the discussion to the simplest case of a single geosynchronous satellite linked to either one or two ground stations. One important consideration for such future space-based operations is the choice of reference oscillator onboard the satellite. We find that with a modestly performing optical reference oscillator and low-power fiber-based frequency combs, quantum-limited time transfer could support intercontinental clock comparisons through a common-view node in geostationary orbit with a modified Allan deviation at the 10^{-16} level at 10-s averaging time, limited primarily by residual turbulence piston noise. In the second application of coherence transfer from ground-to-geosynchronous orbit, we find the system should support high short-term coherence with ~10 millirad phase noise on a 300 GHz carrier at essentially unlimited integration times.

I. INTRODUCTION

Free-space optical time transfer is a technique to disseminate time at the femtosecond level using the coherent exchange of frequency comb pulse trains and, historically, linear-optical sampling to measure the timing.[1] This technique has a demonstrated range of 4–14 km with low power combs[2–5] and out to 113 km with high-power combs.[6] In addition, it is compatible with time-frequency transfer to moving platforms[7,8] as well as three-node geometries.[5] Finally, several papers have identified and analyzed the multiple noise sources that will be present in ground-to-space optical time transfer, including atmospheric anisoplanatism due to transverse satellite motion,[9–12] atmospheric refraction,[13] and residual timing jitter due to the progression of turbulence during the finite time-of-flight from ground to space.[14] However, this previous technique based on linear optical sampling used frequency combs with off-set repetition frequencies and required a received power of a few nanowatts, which effectively precluded its use over the very long links from ground to geosynchronous (GEO) orbit because of the required size/weight and power (SWaP) of any future space-based node. Recently, in contrast, we demonstrated a different comb-based optical time transfer technique that can operate very near the

quantum limit with received powers 10 000× lower than the previous method.[15] This quantum-limited optical time transfer enables operation over the high link losses associated with ground-to-GEO optical links at relatively low launch powers and telescope apertures. In particular, with this new approach, optical time transfer can be accomplished over link losses in excess of 100 dB with only 4 mW of comb power and a modest 10-cm telescope aperture. With this advance in mind, we can consider future missions that exploit space-based optical time transfer at achievable SWaP levels and, therefore, cost.

In a general sense, this quantum-limited optical time transfer can support two different "classes" of problems: (1) absolute time/frequency comparisons between optical atomic clocks, e.g., for redefinition of the second, fundamental physics tests, etc. [Figs. 1(a) and 1(b)], and (2) synchronization of a network of oscillators for distributed coherent sensing, e.g., generating coherent microwaves for a space-based very long baseline interferometry (VLBI) node[16] [Figs. 1(c) and 1(d)]. With these problems in mind, this paper evaluates the expected noise and performance in two specific scenarios: intercontinental time transfer via a geostationary

satellite and coherence transfer from ground to geosynchronous orbit for distributed sensing. We focus on these two applications since they represent the first steps toward much broader timing networks. Furthermore, each does not require the additional development of a state-of-the-art space-based optical atomic clock but can rely on a simpler reference oscillator for the space-based segment, along with other technologies at relatively high technological readiness levels (TRLs), including fiber frequency combs and optical time transfer. Since quantum-limited optical time transfer has not yet been demonstrated at high radial velocities, we do not yet consider satellites in low-earth-orbit (LEO) or mid-earth-orbit (MEO), which will have extremely high radial velocities with respect to a ground station. Only future work will establish if the same time transfer performance is achievable at these high radial velocities, in which case the performance analyses conducted here would carry over.

To ultimately estimate the expected performance of optical time transfer for both intercontinental time transfer via satellite and coherence transfer, this paper is organized as follows: First, in Sec. II, we discuss the choice of a space-based reference oscillator,
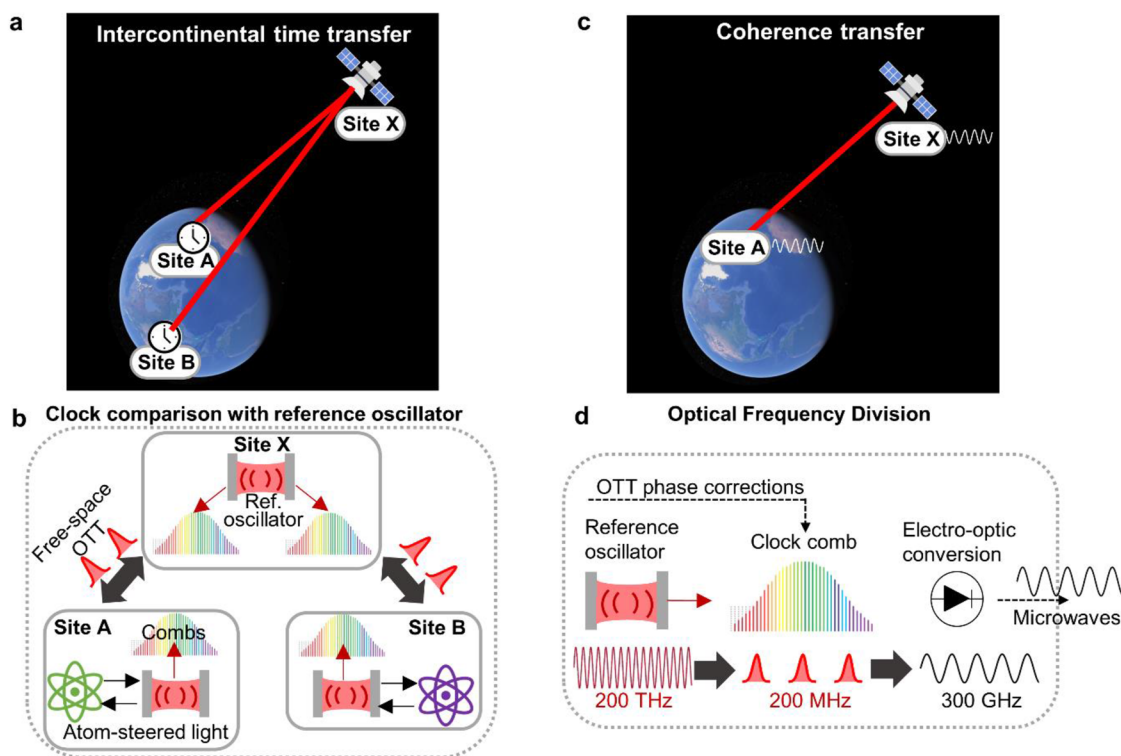

FIG. 1. (a) Intercontinental time comparison between two ground-based optical clocks at sites *A* and *B* via common view two-way transfer to a geostationary satellite, labeled *X*. (b) In the three-node configuration, site *X* has only a reference oscillator, such as a cavity stabilized laser, while sites *A* and *B* have full optical atomic clocks for comparison. At site *X*, the time transfer combs are locked to the cavity stabilized laser light, while on the ground, the combs are locked to the atom-steered light from the optical clocks. A more detailed schematic is shown in Fig. 5. (c) Coherence transfer between a ground site *A* and a geosynchronous site *X* with the two sites generating coherent microwaves. The choice of geosynchronous orbit for this application mirrors current proposals for space-based VLBI nodes[16] and assumes the challenges of increased radial velocity and satellite tracking by the ground station are solvable within the relaxed application requirements compared to intercontinental time transfer. (d) Coherence transfer combines optical frequency division (OFD) to generate low phase noise microwaves at short timescales (<1 s) with optical time transfer (OTT) to track and remove phase offsets at longer timescales (>1 s), either through real-time feedback or in post-processing.

as this is a key system design choice that is common to both use cases. Motivated by TRL levels as discussed above, we restrict any high-performance optical atomic clocks with 10^{-18} level stabilities to ground sites; this scenario is considered more viable in the short term, while low-SWaP clocks are being developed. However, we do consider cavity-stabilized lasers, which have flown in space[17] and recently undergone significant SWaP reductions,[18] and quartz oscillators such as those in Refs. 19 and 20. We evaluate the noise characteristics of potential oscillators in the context of expected holdover periods from turbulence scintillation or processing delays. Based on the analysis given below, we find that both applications require the use of a relatively modest cavity-stabilized laser, as opposed to a quartz oscillator. In Sec. III, we describe the noise sources of free-space optical time transfer and provide their spectral models. Finally, in Sec. IV, we detail how these noise sources will manifest in the two use cases and present relevant expected performance metrics. For the intercontinental clock comparison case, we show it would be possible to compare state-of-the-art optical clocks without penalty other than the unavoidable intermittency due to clouds [e.g., Fig. 5(d)]. For the coherence transfer, we show 10 mrad integrated phase noise between 300 GHz microwaves generated on earth and in space by optical frequency division. At 1 THz, the integrated phase noise would remain below 100 mrad.

For both applications, we consider only the quantum-limited comb-based time transfer approach[15] rather than frequency transfer approaches based on a continuous-wave laser link[21,22] or other comb-based techniques with higher received power requirements.[23] The choice of a phase (time) measurement instead of a frequency measurement is deliberate and enables the greatest functionality possible. For a continuous phase measurement, the sensitivity of the measurement increases with time, at least for white phase noise. Should we then desire a measure of the frequency over a given integration time, we simply take the derivative of the phase measurements, which can be done without introducing excess noise. This is analogous to the advantage of tracking the location of a vehicle by directly measuring its position rather than attempting to integrate the velocity. In addition, because the measured phase is a wrapped (modulo) quantity, we can effectively count the integer cycles to get the integer added level rather than attempting to measure a single quantity that is continuously increasing.

Appendices outline the math used to convert the spectral noise models to the relevant performance metrics (timing uncertainties, Allan deviations, and timing deviations) through either Kalman filter-based analysis or via the well-established phase-noise framework used in Refs. 24 and 25.

Note that we do not focus here on the relativistic effects of time dilation at the geostationary orbit since these are calculable and can be accounted for in post-processing. We recognize, however, that relativistic considerations such as those outlined in Ref. 26 would clearly be important in future satellite-to-satellite time transfer and for future experiments involving space-borne optical atomic clocks.

II. IMPACT OF SPACE-BASED REFERENCE OSCILLATOR CHOICE

A. Introduction

We will discuss the choice of reference oscillator in the context of the intercontinental time transfer sketched in Fig. 5, but many

of the same considerations apply to the coherent transfer system as discussed at the end of this section. At the most basic level, the optical two-way time transfer between site A and the satellite, labeled site X, returns the time difference τ_{AX} between the ground clock and the space-based timescale, set by its reference oscillator. Similarly, the optical time transfer between site B and the satellite returns the analogous time difference, τ_{BX}. In the limit of continuous, noiseless, instantaneous, and simultaneously measured time differences, we can construct the time difference between the clocks at sites A and B as $\tau_{AB} = \tau_{AX} - \tau_{BX}$, where the timing of the reference oscillator drops out entirely, in which case almost any reference oscillator will suffice. (Hence, the advantage of common-view time transfer.) However, in reality, there will be fixed and/or varying time delays between the two measurements, τ_{AX} and τ_{BX}. These delays may be on the order of milliseconds due to turbulence driven scintillation and signal processing delays, including electronic and optical path length drifts, or on the order of minutes to hours due to clouds [Fig. 4(b)]. A sufficiently high-quality reference oscillator can "holdover" the timing between asynchronous measurements. A more complete analysis is provided later in this section and Appendix C, but we can assume the quantity τ_{AX} is evaluated at time t and τ_{BX} is effectively evaluated at some later time $t + t_h$, where t_h is the holdover time. The difference between these measurements has an error term added to the desired A-to-B clock time, τ_{AB}, that depends on the reference oscillator,

$$\tau_{AX}(t) - \tau_{BX}(t + t_h) = \tau_{AB}(t) - \delta\tau_X(t_h), \quad (1)$$

where $\delta\tau_X(t_h)$ is the residual time wander of the reference oscillator over the holdover time t_h due to its stationary phase/frequency noise. Its derivative gives the residual noise of any frequency comparison.

The choice of the reference oscillator then represents a trade between this time wander and the size, weight, and power (SWaP) of the reference oscillator. As discussed above, we will limit our
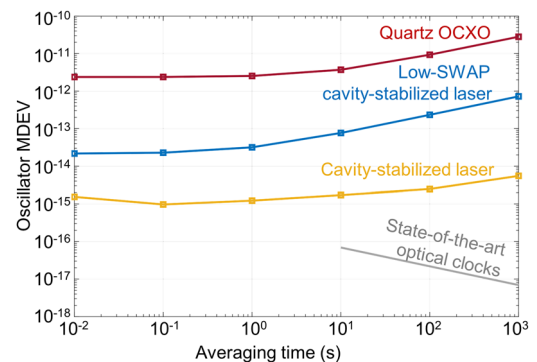

FIG. 2. Fractional frequency instability (MDEV) for the three example reference oscillators used in the analysis. These modified Allan deviations are calculated directly from the frequency noise power spectral density values given in Table I. Those values, in turn, are estimated based on available phase noise or Allan deviation values provided for Quartz in Ref. 19; the cavity-stabilized laser of ~8 cm in length in Refs. 27 and 28; and the miniaturized, 6 mm-long cavity-stabilized lasers in Ref. 18. The state-of-the-art optical atomic clock is based on an ADEV scaling of $3.1 \times 10^{-16}/\sqrt{\tau}$ with a flicker floor of 5×10^{-19}, which is scaled to MDEV for this figure. These instabilities are intended to be representative of these technologies rather than specific systems.[20]

TABLE I. Fractional frequency noise power spectral density coefficients for the representative reference oscillator technologies shown in Fig. 2. The fractional frequency noise power spectral density model is given by $S_y = h_{-2}f^{-2} + h_{-1}f^{-1} + h_0 + h_1 f + h_2 f^2$, with units of 1/Hz, where f is the Fourier frequency. Additional terms are also indicated where appropriate. All values here are intended to be representative of these technologies in general, rather than any specific implementation. In all three categories, advanced designs can certainly decrease the noise coefficients, but this advance should be balanced by tradeoffs in robustness and SWaP for space-based operation.

Oscillator	Random walk frequency noise, h_{-2}	Flicker frequency noise, h_{-1}	White frequency noise, h_0	Flicker phase noise, h_1	White phase noise, h_2	Additional S_y terms
RF (quartz) f_c = 100 MHz	1.5×10^{-25}	6×10^{-24}	$\cdots$	4×10^{-29}	$\cdots$	$\cdots$
Miniaturized cavity-stabilized laser f_c = 200 THz	1×10^{-28}	5×10^{-28}	$\cdots$	$\cdots$	5×10^{-40}	$\cdots$
Cavity-stabilized laser f_c = 280 THz	8×10^{-33}	1×10^{-30}	8×10^{-32}	$\cdots$	$\cdots$	$1 \times 10^{-41} f^{-4}$

consideration to technologies that have flown into space or could in the near future. Choices include. RF/microwave oscillators (e.g., quartz or dielectric resonator oscillators), optically based oscillators/clocks such as cavity-stabilized lasers,[17,18,27,29,30] iodine clocks,[31] or two-photon Rubidium clocks,[32,33] all of which are under development for space-based operation. Figure 2 and the corresponding Table I give performance metrics for the quartz oscillator and two cavity stabilized lasers chosen here as representative examples. The phase noise of the quartz oscillator is well established, and we use the typical values of a commercially available oven controlled crystal oscillator (OCXO).[19] For the larger cavity-stabilized laser, we have selected parameters that follow the performance of the cavity-stabilized laser flown on the GRACE-FO mission.[17,27,28] Certainly, even higher performance cavity-stabilized lasers have been developed for the laboratory. Although not included here, we note that the iodine clock intended to fly on the COMPASSO mission[31,34] closely follows the performance of the cavity-stabilized laser in Ref. 27 and represents the state-of-the-art for an atom-based clock that uses neither an optical cavity nor laser cooling. We also include the relatively modest parameters of a miniaturized cavity-stabilized laser,[18] which represent the trade-off in performance for SWaP in the case of a cavity-stabilized laser.

B. Origin of holdover time

Before evaluating the residual time wander in Eq. (1), we explore the origin of the holdover time, t_h, in the context of a ground-to-space coherent optical link. Here, we are broadly defining holdover time as a period of delay or interruption between active time transfer measurements during which the reference oscillator will drift in frequency and phase. Generally, the effective holdover time can arise from different effects, each with different characteristic durations. First, turbulence-induced scintillations can cause intermittent signal fades on either link. Their frequency and duration are reduced by increasing the comb output power or telescope aperture, but the power-aperture product is a very strong driver of overall mission cost. Reference 15 provided statistics on signal fades near the threshold at strong turbulence levels across a 300-km horizontal link, likely worse than a link to geostationary orbits. The fades are generally of a millisecond or shorter duration, although they can extend beyond 10 ms. The optical time transfer processing incorporates Kalman filter-based prediction algorithms to "ride over" these short fades and thereby output a continuous measure of the clock time difference $\tau_{A(B)X}(t)$. However, the prediction error of this filter

sill yields the added noise term $\delta\tau_X(t_h)$, where the effective holdover time is just the fade duration on a single link.

Processing delays represent a second possible contribution to the effective holdover. The processing delay will be related to the coherent signal integration time, the communication rate of various timing signals, and asynchronous operation between the two links. In the current system, it is on the order of milliseconds or less, and presumably, a similar value is achievable with the appropriate design of the space-based instrument onboard the geostationary satellite.

Figure 5 assumes that the geostationary satellite includes two free-space optical (FSO) terminals, one dedicated to each link. One could also consider the time-multiplexed use of a single free-space optical terminal, in which case the holdover time would be 10s of seconds at a minimum to cover the physical link acquisition, re-acquisition of the incoming comb signals by the tracking comb, and initiation of the optical two-way time transfer protocol. Similarly, shared use of the FSO terminals with other applications, such as a high-speed data link or time-transfer downlinks, would lead to minutes-to-hours of potential holdover time.

Finally, cloud cover can have a significant impact on optical ground to satellite links through scattering and attenuation. For an intercontinental clock comparison using optical links between two ground stations and a geostationary satellite, cloud cover at either ground station will interrupt the comparison. To estimate the duration and frequency of the cloud-induced interruptions for a clock comparison, we consider time transfer between Boulder, CO, and Europe. (A similar analysis could be conducted, for example, from Boulder, CO, to Tokyo, Japan.) In Europe, the clock comparison fiber network between Braunschweig (PTB), Paris (SYRTE), and London (NPL)[35] allows the use of one of multiple ground stations to increase the chances of having a clear line of sight to the satellite.

Figure 3 shows an example of a clear sky mask for a 48-h period in 2022 at a 15-min time resolution, as well as the weekly percentage of clear skies for 2022 for Boulder, Paris, London, and Braunschweig. For 34% of the time, the sky was clear in Boulder and either Paris, London, or Braunschweig. These mutually clear periods were on average 2 h in length, and the maximum duration was 2 days. During the remaining 66% of the time, one would expect link interruptions due to cloud cover. These interruptions were, on average, 4 h and, maximally, 3 days long.

C. Magnitude of $\delta\tau_X(t_h)$

With these very different holdover times in mind, we now evaluate $\delta\tau_X(t_h)$ as a function of holdover time with a Kalman-filter
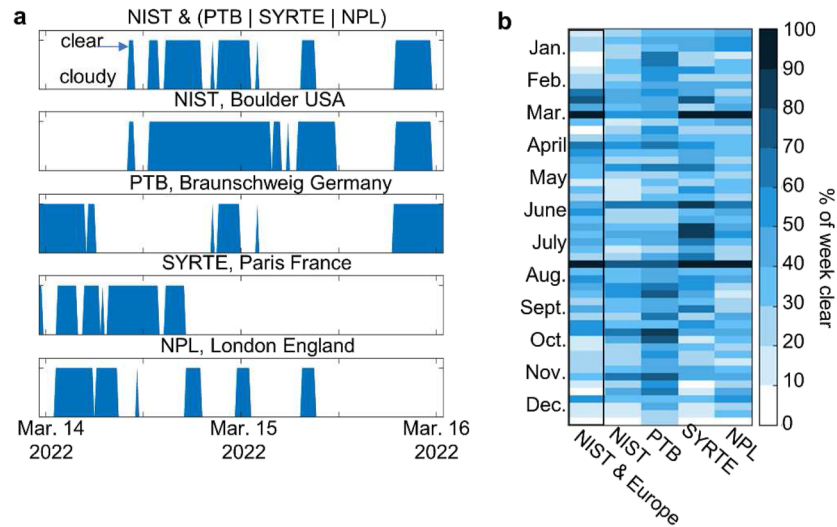
FIG. 3. Clear sky cover. (a) Example clear sky mask for a 48-h period in 2022 at 15-min resolution. The top plot shows combined periods with a clear sky for both NIST in Boulder and either PTB in Braunschweig, SYRTE in Paris, or NPL in London. The lower plots show the clear sky mask for each location individually. The clear sky data are from EUMETSAT Meteosat SEVIRI[36] for Braunschweig, Paris, and London, and from NOAA GOES ABI for Boulder.[37] (b) Weekly clear sky percentages in 2022 for the combined mask as well as individual ground stations.

based predictor. The Kalman-filter approach has two benefits. First, it mirrors the real-time processing that would occur on board the satellite to deal with such signal dropouts. Second, the Kalman filter provides the optimum predictor and quantified uncertainty, which is exactly $\delta\tau_X(t_h)$ in this case. However, to connect with parameters typically used by the time-frequency community to characterize time-frequency transfer, we also evaluate the effect of the holdover

time in terms of the contribution to the modified Allan deviation (MDEV),

The Kalman filter analysis is described in detail in Appendix A and is generally applicable to any reference oscillator. Appendix B also provides the basis for the MDEV analysis. The results of the Kalman-filter analysis for $\delta\tau_X(t_h)$ for the three specific oscillators in Table I are shown in Fig. 4(a). In general, the time wander increases
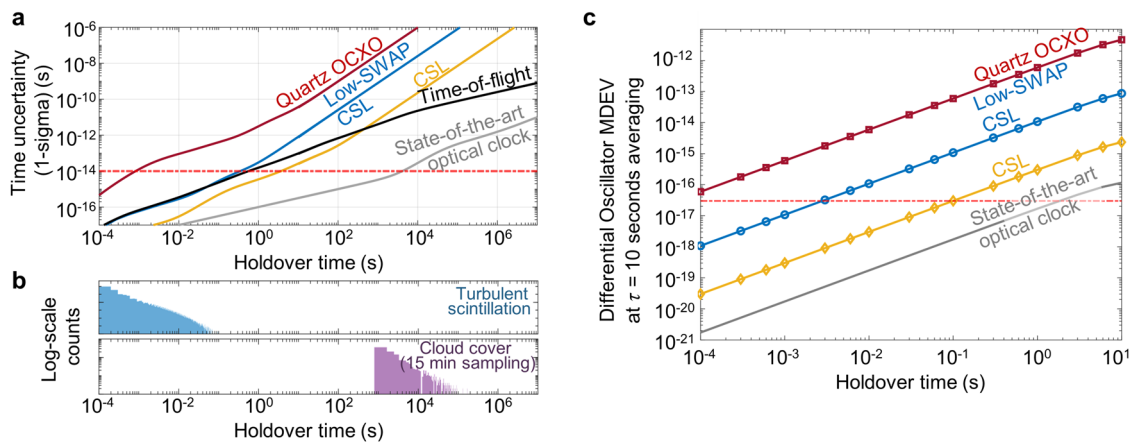

FIG. 4. (a) Time uncertainty, $\delta\tau_X(t_h)$, as a function of holdover time, t_h, for the three reference oscillator options of quartz OCXO (red), a low-SWaP cavity stabilized laser (CSL) (blue), and a larger cavity stabilized laser (yellow). In addition, the time-of-flight uncertainty due to turbulence phase noise (black) and $\delta\tau_X(t_h)$ for a state-of-the-art laboratory-based optical atomic clock (gray)[38] are also shown. Finally, a nominal target 1-sigma, 10 fs uncertainty is shown as a red dashed line. (b) Histograms of turbulent-induced signal loss due to scintillation and cloud cover for the Boulder to Europe (Braunschweig, London, or Paris) link. Scintillation data are from Ref. 15 using a 4-h dataset with the same 270 fW threshold assumed for the ground-to-GEO model. (c) Fractional frequency instability (MDEV) of the differential oscillator noise for the three reference oscillators (and a state-of-the-art optical clock) as a function of holdover time. A nominal target MDEV of 3×10^{-17} at 10 s is shown as a red dashed line.

as $\sqrt{t_h}$ initially for white frequency noise and then increases as t_h for flicker and random walk frequency noise. Figure 4(c) shows the residual MDEV for different delays (holdover times) for each oscillator.

D. Space-based reference oscillator choice

Finally, we can make a selection of the space-based reference oscillator. For the case of intercontinental time transfer, to keep pace with the performance of state-of-the-art optical clocks,[39–41] we assume future optical clocks at both nodes with MDEV white frequency noise scaling of $1 \times 10^{-16}/\sqrt{\tau}$ and a flicker floor of 5×10^{-19}. Thus, we set a target goal of limiting the time wander to less than 10 fs and the MDEV to below 3×10^{-17} at 10-s averaging time. With those goals in mind, it is clear that an effective holdover time of $t_h < 100$ ms is tolerable if the space-based reference oscillator is a larger cavity-stabilized laser. Even if the low-SWaP cavity-stabilized laser is used, an effective hold-over time of <2 ms is tolerable. However, for a quartz oscillator, we would need $t_h < 100$ μs. Given that a cavity-stabilized laser has flown,[17] in the absence of severe SWaP restrictions, it is the obvious choice to enable intercontinental time transfer. Based on the typical turbulence-induced fade frequency in Fig. 4(b), we note that for ~2% of the time, these fades will exceed the tolerable maximum holdover time of ~2 ms for the lower SWaP cavity-stabilized laser. Since this slight penalty in uptime allows for a significant reduction in system SWaP, we present the projected performance of intercontinental time transfer in Sec. IV A using this miniaturized cavity-stabilized laser.

For the case of the coherent network, we consider the slightly relaxed target goals of 100 fs wander and an MDEV to be below 3×10^{-15} at 10-s averaging time. We note here that again, the obvious choice of a reference oscillator is a cavity-stabilized laser, but that here the performance of the much lower SWaP miniaturized cavity-stabilized laser is sufficient for an effective holdover time of $t_h < 300$ ms. With this tolerable holdover time, we again consider just the miniaturized cavity-stabilized laser for the analysis of the coherence transfer performance in Sec. IV B. This application presents an interesting trade-off in size/weight and power in terms of the optical frequency division (OFD) and optical time transfer (OTT) systems. For example, a larger state-of-the-art optical cavity-stabilized laser system could provide very low phase-noise microwaves on its own, but the addition of OTT drops the performance requirements and, therefore, the SWaP envelope of the cavity-stabilized laser system significantly. The ultimate system design for a future mission will depend on the exact requirements and SWaP tradeoffs.

As we noted above, in both scenarios, we consider two-way time (phase) transfer. Counterintuitively, although none of the reference oscillators considered here can provide a holdover across the tens of seconds that might be associated with multiplexed use of a FSO terminal or with cloud cover, this will not prevent successful clock comparisons or synchronization. In the case of the intercontinental comparison, a long duration dropout on either link will block the two-way time transfer measurements; however, once both links are re-established, we directly measure any overall accumulated time drift that occurred during the dropout, assuming neither site has phase-slipped during the dropout. In other words, due to the use of time transfer instead of a frequency comparison, that measurement time is not "lost," and we can still evaluate the average frequency difference between the clocks, resynchronize when the link is established, and track the elapsed time during these intervals.

III. NOISE SOURCES BEYOND THE REFERENCE OSCILLATOR

We now turn our attention to the other relevant noise sources present in the two-way comb-based optical time transfer. This discussion provides the framework to finally analyze the overall expected performance of either the intercontinental clock comparison or the coherence network. These noise sources include fundamental shot noise, phase noise associated with the stabilization of the frequency combs, environmentally induced noise on out-of-loop fiber optic paths, and differential noise arising from system delays. These differential noise terms include not only the differential reference oscillator noise discussed above but also differential time-of-flight (piston) noise, both due to temporal and spatial turbulence variation. Here, we will discuss each of these noise terms in detail. The values used are mainly derived from the high-loss, quantum-limited OTT experiments in Ref. 15. Since our performance metrics for both applications are in time or phase, all noise sources are described with timing power spectral densities (PSDs).

A. Fundamental shot noise

Reference 15 demonstrated optical time transfer at the photon shot-noise limit, and we assume a similar time transfer system here. The shot-noise contribution to a one-way timing measurement will have a white timing PSD of magnitude,

$$S_{sn} = \frac{\tau_p^2}{2 \ln(2)^2 \eta} \left(\frac{h\nu}{P_{rec}} \right) \quad (s^2/\text{Hz}), \qquad (2)$$

where τ_p is the full-width half maximum pulse width, $h\nu$ is the photon energy, and P_{rec} is the optical power from the incoming clock comb light received by a detector with quantum efficiency η. Here, we conservatively assume a P_{rec} of 270 fW, corresponding to a 102 dB loss for a 4-mW transmitted clock comb power, and a τ_p of 355 fs. In practice, there may be an additional multiplicative penalty due to differential pulse chirp and system non-idealities (this penalty was ~3 in Ref. 15).

B. Frequency comb noise

The comb-based optical time transfer system described here is based on fiber frequency combs stabilized by two phase locks: the carrier envelope offset lock with residual phase noise S_{ceo} (rad²/s) and a lock between the mth comb tooth and the reference oscillator (cavity-stabilized laser) with residual phase noise S_{opt} (rad²/s). The resulting timing noise PSD for a given comb is

$$S_{comb} = \frac{S_{opt} + S_{ceo}}{(2\pi m f_r)^2} \quad (s^2/\text{Hz}), \qquad (3)$$

assuming uncorrelated noise between the two locks. As shown in Appendix C 5, empirical measurements of our field-deployed, robust comb system yield an approximate PSD model of

$$S_{comb} = 1 \times 10^{-45} f^2 + 1 \times 10^{-40} f^{1/2} \quad (s^2/\text{Hz}), \qquad (4)$$

where f is the Fourier frequency for $f < 10^5$ Hz, which is the approximate bandwidth of the carrier envelope offset frequency lock. Beyond 10^5 Hz, the PSD decreases following $5 \times 10^{-20} f^{-3}$.

C. Environmental noise

Despite temperature control of the transceivers, some residual temperature drifts in optical fibers within the comb system will exist, which will induce length and refractive index changes that give rise to timing fluctuations. Many fibers are considered in-loop for the two comb phase locks described above, so the environmentally induced timing fluctuations in these fibers will be negligible. Other fibers in the system, however, will be subject to these fluctuations. From measurements of the system in Ref. 15 and assuming a 1×10^{-19} MDEV flicker floor, as demonstrated in Ref. 6, we estimate environmental timing noise to be

$$S_{env} = 10^{-35} f^{-2} + 3.6 \times 10^{-40} f^{-3} \quad (\text{s}^2/\text{Hz}). \quad (5)$$

If we assume 1 m of out-of-loop fiber, this corresponds to 100 mK of integrated temperature noise over 24 h. For 10 m of fiber, this would be restricted to 10 mK of integrated noise.

D. Time-of-flight noise

Two-way time transfer is based on the concept of the reciprocity of a bi-directional link, which allows for the combination of two separate one-way measurements to cancel the time-of-flight contribution and return only the time difference between the two sites. However, partial reciprocity will result in an incomplete suppression of the noise due to time-of-flight fluctuations, whether due to a spatial or temporal separation of the one-way measurements.

Fluctuations in the time-of-flight of the comb pulses may arise from both atmospheric turbulence and platform motion. In the limit of weak turbulence—the case for all but the most extreme slant paths—atmospheric turbulence can be characterized by the standard Kolmogorov power spectrum, which results in a $f^{-8/3}$ Fourier frequency scaling of the timing noise PSD, $S_{turb}(f)$.[42–44] Here, to model the vertical profile of the refractive index structure parameter, we assume a Hufnagel–Valley profile[42] with a ground level refractive index structure parameter of $C_n^2 = 10^{-14}$ $(\text{m}^{-2/3})$ at an elevation angle of 45° from a height of 10 m, which yields $S_{turb}(f = 1 \text{ Hz})$ $= 1.7 \times 10^{-29}$ (s^2/Hz). For a ground-to-GEO link, the upward and downward traveling pulses will not pass through the atmosphere simultaneously but rather with a delay, t_{delay}. With this delay, and assuming lumped turbulence close to the ground, the turbulence-induced delays do not fully cancel for the two-way time transfer, so the noise PSD has a differential turbulence noise term,

$$S_{dturb} = 4 \sin^2(\pi f t_{delay})(1.7 \times 10^{-29}) f^{-8/3} \quad (\text{s}^2/\text{Hz}). \quad (6)$$

(See Appendix B 2 for the derivation of the differential transfer function.) While, in principle, this delay could be tuned to pair pulses that pass simultaneously through the atmosphere, here we choose to set $t_{delay} = TOF$, where the quantity TOF is the one-way time-of-flight of 120 ms, which, in effect, means we are combining the timing of pulses that are simultaneously launched from their respective sites. This has implications for the impact of platform motion, which is discussed in Appendix C 2.

For an eventual extension to ground-to-LEO, ground-to-MEO, or ground-to-cislunar links, the impact of turbulence anisoplanatism[9–12,14] must also be considered, which will result in an additional filtered noise contribution from the turbulence timing PSD.

IV. DETAILED DESCRIPTION OF EXPECTED PERFORMANCE

A. Intercontinental time transfer

The intercontinental time transfer, illustrated in Fig. 5, would enable the dissemination of the redefined second[45] from clocks in the US (in Boulder, CO, or Washington DC) to the fiber-networked clocks in Europe or Japan.[46,47] By creating intercontinental-spanning ground-based clock networks, it would also enable fundamental physics tests.[48–59] For example, a comparison of optical clocks at nearly opposite locations on the earth can probe relativity due to the differential gravity from the sun.[57,58,60] Intercontinental time transfer would also enable clock-based geodesy by connecting a portable clock to a national metrology institute (NMI), enabling widely spaced absolute geodetic reference points.[49] Finally, when low-SWAP optical atomic clocks are developed for space-based instruments, the performance of this ground-to-satellite-to-ground clock comparison will clearly carry over to future ground-to-satellite clock comparisons.[48,60–63]

Figure 5(a) outlines a schematic of intercontinental time transfer via a common view to a geostationary satellite. For this and the following cases, we assume that the optical time transfer is frequency-comb-based using the quantum-limited approach of Ref. 15, which relies on the recently developed time programmable frequency comb.[64] Following the previous discussions, we assume a miniaturized cavity-stabilized laser as the reference oscillator on the satellite and the existence of a dedicated free-space optical terminal for each link to the ground. From a SWaP and TRL argument, these combs will necessarily be based on modelocked fiber lasers, as in Ref. 15, and can additionally exploit the low-power and more radiation-insensitive waveguide designs for carrier-envelope offset detection.[65,66] The comb-based optical time transfer has an implicit ambiguity of $0.5/f_r$, where f_r is the comb repetition rate. To remove this ambiguity, we assume the existence of coarser time synchronization and ranging that is good to ≈1 ns—this drives the system toward frequency combs with $f_r \approx$ 100–200 MHz.

Equation (1) outlines the concept where the two two-way time offsets are subtracted to yield the time offset between clocks A and B. Appendix C 3 gives a more complete noise analysis that includes the noise terms given above and their suppression through the two-way operation. We find the following expression for the total timing noise PSD corresponding to the residual noise on the clock time comparison between sites A and B,

$$S_{\Delta\tau AB} = 2S_{comb} + 2S_{env} + S_{sn} + \frac{1}{2}|H_{diff}(t_h)|^2(S_{osc})$$
$$+ \frac{1}{2}|H_{diff}(TOF)|^2 S_{turb}, \quad (7)$$

where S_{osc} is the timing noise PSD of the space-based reference oscillator (see Table I for the corresponding fractional frequency noise PSD). The shot noise contribution, S_{sn}, is given by Eq. (2), assuming a weak 270 fW signal. We assume similar noise performance for
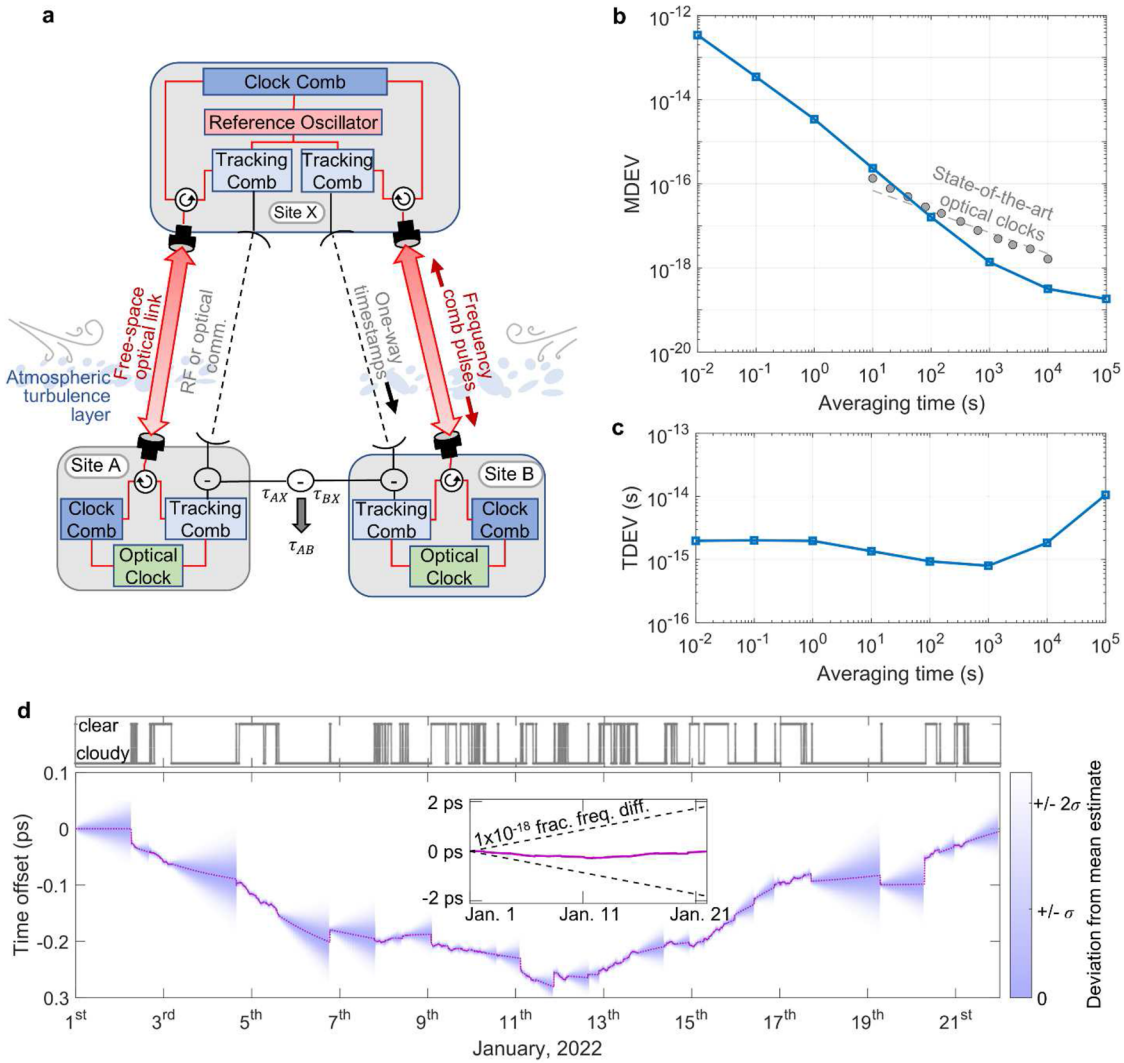
24 July 2024 10:18:38

FIG. 5. Intercontinental time transfer. (a) The three-node configuration uses bi-directional optical time transfer between the two ground sites and the space-node, site X. Each site transmits the optical pulse train from its own clock comb and receives the optical pulse train from the opposite site. The timing of this incoming pulse train is compared to the local timescale by using a tracking comb for quantum-limited detection. The results of the one-way timing measurements are sent over either an RF or optical communication link to the opposite site, where a two-way subtraction yields the relative time and frequency offsets between the respective ground sites and satellite, τ_{AX} and τ_{BX}. A further two-way subtraction of these time offsets yields the relative time and frequency between the ground clocks, τ_{AB}. Here, we assume both ground sites are referenced to a state-of-the-art optical atomic clock, while the satellite uses a lower performance optical reference oscillator. (b) The projected modified Allan deviation (MDEV) for the system parameters selected in this paper, which are based on currently available, demonstrated technologies. At a 10-second average, the MDEV reaches 2×10^{-16}. This projection assumes using a low-SWaP cavity stabilized laser as a reference oscillator at site X.[18] State-of-the-art optical clock curve (dashed gray) follows $3.1 \times 10^{16}/\sqrt{2}\ \tau^{-1/2}$ along with measured points from a clock comparison.[38] (c) Corresponding time deviation. (d) Example realization of 3 weeks of intercontinental time transfer noise (pink) and uncertainty (purple colormap) generated by combining Kalman filter analysis (Appendix A) and satellite data of cloud cover between Boulder and Europe from January 2022 (gray traces at top). The noise model used in the Kalman filter and for the time series realization is described by the time transfer PSD shown in Fig. 6. During clear sky periods, the time series is fed into the filter as observations, while during cloudy periods, the filter estimates the noise without observation, and the estimated uncertainty grows. Due to the precision of the time transfer system, the estimated uncertainty collapses rapidly with a single clear sky period. This noise realization represents an example of a measured intercontinental time transfer signal for perfect ground clocks with no drift and a flicker floor of 10^{-19} for the time transfer. In practice, the signal will also include noise from the clocks, which should dominate over longer time scales, as shown in (b). The inset gives a sense of scale for the projected time offset (dashed lines) between two clocks with a fractional frequency offset of 1×10^{-18}.

all combs, S_{comb}, given by Eq. (4), and similar environmental noise, S_{env}, at all sites given by Eq. (5). $H_{diff}(t_{delay})$ is the transfer function to account for the partial suppression of the reference oscillator and turbulence noise by use of common view and two-way time transfer,

respectively (Appendix B 2). For the differential reference oscillator noise, we allow for effective holdover times of up to $t_h = 1$ ms. In other words, we assume that we can compute τ_{AB} if the measurements of τ_{AX} and τ_{BX} are made within 1 ms of each other. If
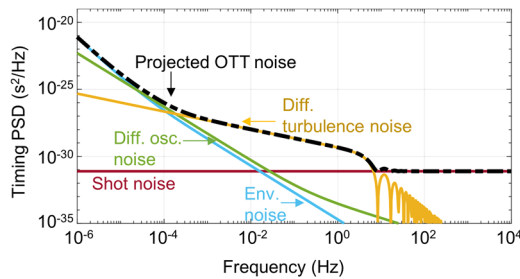
FIG. 6. Power spectral density (PSD) of time transfer noise on the intercontinental clock comparison in the absence of clouds. This PSD is used to calculate the projected MDEV and TDEV in Fig. 5. As described in the text, the analysis includes contributions from shot noise (red line), differential reference oscillator noise assuming a holdover time of 1 ms, and the low-SWaP laser cavity in Ref. 18 (green line), differential turbulence assuming a delay time equal to the 120 ms time-of-flight, and the turbulence spectrum estimated in Sec. III D (orange line) and the environmental noise estimated in Sec. III C (blue line). The residual frequency comb noise estimated in Sec. III B is too low to appear in this plot. The sum of these noise sources, according to Eq. (7), is the projected OTT noise (dashed black).

this is not the case, we assume we have a fade and resume computation of the phase offset when the measurements of τ_{AX} and τ_{BX} are made within 1 ms of each other. Figure 6 shows the magnitude of the different contributions along with their sum.

With this timing noise PSD, we can calculate the modified Allan deviation and time deviation[24,25] shown in Figs. 5(b) and 5(c) and

create an example realization of intercontinental time transfer noise shown in Fig. 5(d). In the absence of clouds, the projected performance across the entire link (including both two-way time transfer links) is given by Figs. 5(b) and 5(c). This performance is based on existing demonstrations using currently available technologies and is limited by differential piston noise from turbulence at short timescales and by environmental flicker noise at longer timescales (Fig. 6). Clouds will interrupt the links but, assuming continuous operation of the ground-based clocks, will not interrupt the time comparison itself, as any difference in elapsed time is immediately quantified when the clouds break. Figure 5(d) shows a time series realization of time transfer noise and uncertainty through these cloudy periods, as estimated by a Kalman filter. During a period of cloud cover, the Kalman predicted uncertainty grows, only to be rapidly reduced to the nominal 30-fs 1-sigma uncertainty for the OTT measurement when the clouds break over both sites. For this analysis, as discussed earlier, we assume one clock is in Boulder and the other is at any one of three sites in Braunschweig, Germany, Paris, France, or London, UK, where we assume there is a subsequent transfer of timing information across Europe over a ground-based fiber network.[35] A similar calculation can be performed for clock comparisons between Japan and Europe or Boulder and Japan.

B. Coherence transfer system

Figure 7 illustrates the second scenario considered of coherence transfer to enable very long baseline interferometry or other
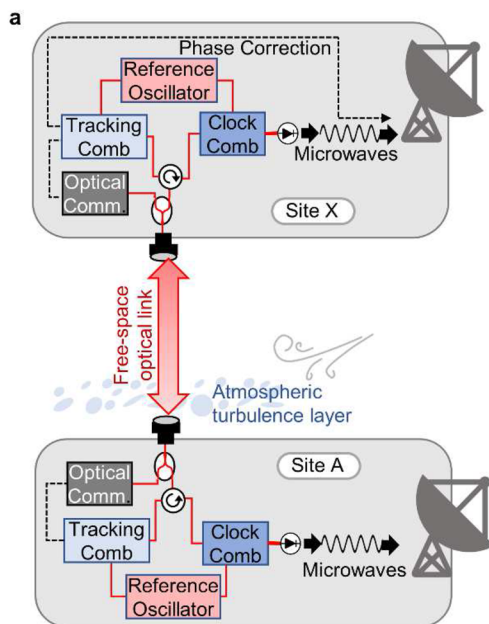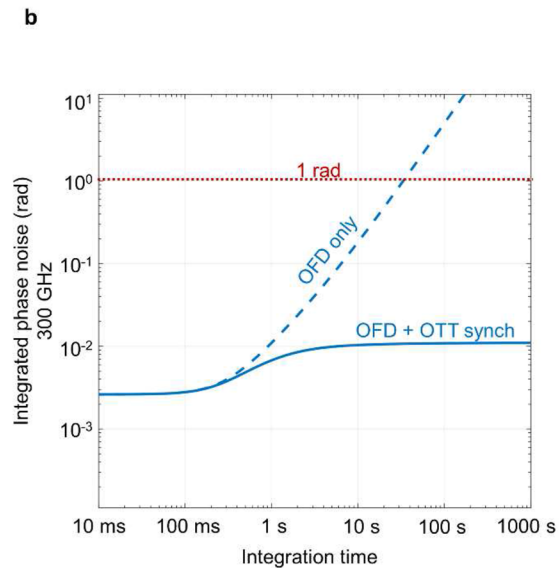

FIG. 7. (a) As in Fig. 5, the OTT is based on the bi-directional transmission of the pulse train from a clock comb, followed by tracking-comb based detection of the incoming signals. The two-way subtraction of the timing signals yields the time/phase offset between the microwave signals at each site. As this application will require a high bandwidth optical communication link for data transfer, we assume the OTT system would be wavelength multiplexed onto this optical communication channel. (d) The coherence, as quantified by the integrated variance of the phase noise between the microwave signals at each site vs integration time. As the system maintains constant timing noise, the integrated phase noise scales linearly with the carrier frequency, which is equal to 300 GHz here. At short integration times (<1 s), the coherence is set by the OFD system, limited here by frequency comb lock residuals and the photodetection noise floor. Beyond 1 s, OTT maintains a nearly flat integrated phase noise of 10 mrad, limited by differential turbulence noise.

distributed coherent sensing techniques in space.[16,67–69] Here, we consider the simplest case of only one site on the ground and in space, mirroring current proposals for an Event Horizon Explorer mission,[16] which seeks to extend the striking measurements of black hole formation and dynamics by the existing Event Horizon Telescope.[70–77] Here, the goal is to generate a microwave signal in space that is phase coherent with a microwave signal on the ground through the combination of optical frequency division (OFD) and optical time transfer (OTT). In this case, the combined inclusion of a cavity-stabilized laser and frequency comb is doubly useful. In OFD, one exploits the low phase noise achievable with a cavity-stabilized laser; the frequency comb acts as an almost perfect frequency divider to output microwaves at any harmonic of the comb repetition frequency via photodetection of the clock comb's optical pulse train[78] [see Fig. 1(d)]. The OFD alone provides low phase noise microwaves at short times. At longer times, this phase will wander. Therefore, we implement OTT to synchronize the two sites at longer times, thereby maintaining phase coherence between the ground and geostationary satellite, as illustrated in Fig. 7(a).

Ultimately, future space-based very long baseline interferometry (VLBI) would require multiple satellites and other orbits, but here we again restrict the analysis to an initial simplified scenario with a single ground station and single geostationary satellite for the purposes of analyzing the system performance. Furthermore, such an application will require a high bandwidth link for data transfer, which will in turn require free-space optical (FSO) terminals linking the geostationary satellite and ground station. The OTT can then simply "piggyback" on this link. In the event of cloud cover, both data communications and coherence transfer will be simultaneously interrupted. Both to avoid extensive cloud cover and to reduce turbulence, the ground station would likely be at high altitudes. In the event of shorter ms-level turbulence-induced signal fades, it is assumed the OTT would use a Kalman filter predictor to holdover the phase (and the data communication would use a buffer).

There is a subtlety in whether the phase synchronization is done in real-time or in post-processing. In Ref. 15, the two timescales were fully synchronized in real time by feeding back their time offset, as measured by the OTT, at site X. Such synchronization is possible here as well, but the real-time feedback bandwidth is limited by the longer 120 ms time-of-flight to about $(8TOF)^{-1} \approx 1$ Hz. If needed, the OTT signals can still provide the necessary phase corrections on shorter timescales in post-processing where the time-of-flight delay is not an issue. In fact, such an approach mirrors current VLBI systems where the data at each site is recorded using the local hydrogen masers and combined only afterward in post-processing, where many additional adjustments to the phase are needed in any case. For the parameters considered here, however, we find a synchronization bandwidth of about 1 Hz would optimize the phase coherence, giving the user the choice of implementing active feedback to synchronize the two sites or using a post-processing approach.

A similar analysis to the intercontinental clock comparison, outlined in Appendix C 4, yields the timing noise PSD for the OTT measurement between the ground and space-based oscillators as

$$S_{\Delta\tau AX} = S_{comb} + S_{env} + \frac{1}{2}S_{sn} + \frac{1}{4}\left|H_{diff}(TOF)\right|^2 S_{turb}, \quad (8)$$

where we have again assumed similar noise performance of the combs and similar environmental noise across sites. The microwave signal is generated by the photodetection of the clock comb pulse train on the space segment. The timing noise on these microwaves can be written as

$$S_{\mu wave} = |H_{corr}|^2 S_{\Delta\tau AX} + |1 - H_{corr}|^2 (S_{osc} + S_{comb}) + S_{photodetection}, \quad (9)$$

where H_{corr} is the closed loop phase correction transfer function that reflects the synchronization, or phase correction, of the reference oscillator based on the OTT measurement. Here, we assume a synchronization bandwidth of $(8TOF)^{-1} \approx 1$ Hz based on the projected noise components. Furthermore, we modeled H_{corr} as a two-pole low pass filter. The additional shot noise and timing jitter contributions from the photodetection process are studied,[79] and here they are represented by the additional timing PSD $S_{photodetection}$. We use values for this noise term based on Ref. 80.

The timing phase noise can be converted to the single sideband phase noise for a given microwave carrier frequency, f_c, through the usual transformation $L(f) = 4\pi^2 f_c^2 S_x(f)/2$, where f is the Fourier frequency. Note that this phase noise PSD will scale quadratically with the carrier frequency.
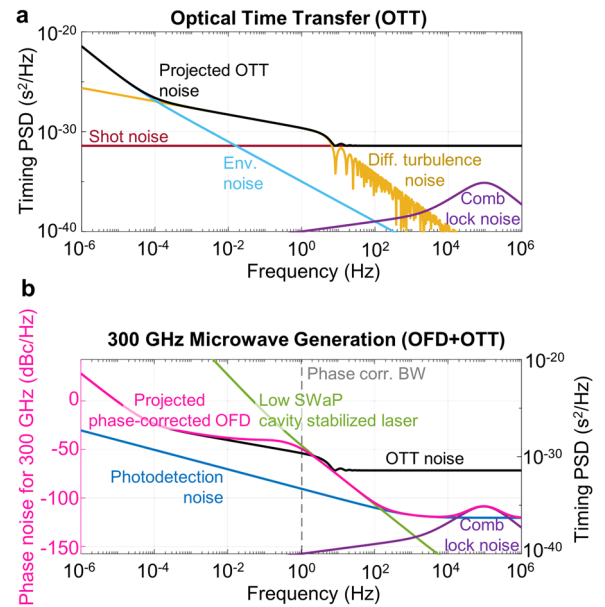

FIG. 8. Power spectral densities of time transfer and 300 GHz microwave generation via optical frequency division for the coherence transfer system outlined in Fig. 7. (a) Projected timing noise for two-way time transfer (black line) along with individual contributions from Eq. (8), including differential turbulence noise (orange line), environmental noise (blue line), shot noise (red line), and comb noise (purple line). (b) Projected single sideband phase noise, $L(f)$, for 300 GHz microwaves (pink line) along with the individual contributions from Eq. (9), including the reference oscillator phase noise (green line), the OTT noise (black line), the photodetection noise (blue line), and the comb noise (purple line). The corresponding timing noise is given on the right axis. The phase corrected OFD curve was used to generate the integrated phase noise plots in Fig. 7(b).
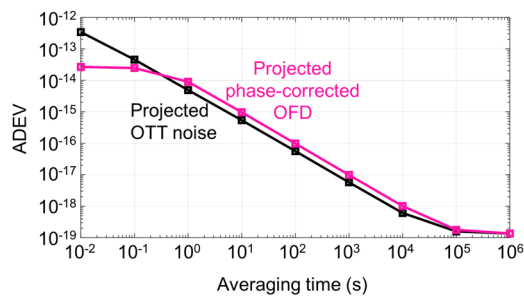
FIG. 9. Fractional frequency instability (ADEV) for the coherence transfer system. The fractional frequency instability given by the Allan deviation (ADEV) for time transfer between site A and site X (black) scales at $5.9 \times 10^{-15}\tau^{-1}$ before reaching a flicker floor of 1.4×10^{-19}. Similarly, the OFD phase corrected with the time transfer (pink) scale of $9.0 \times 10^{-15}\tau^{-1}$ before reaching the same flicker floor. This carrier independent metric can be used to project the expected loss of coherence for any choice of OFD plus OTT generated microwave frequency.

Figure 8(a) provides the timing noise PSD for the optical time transfer with the contributions from the terms of Eq. (8). Figure 8(b) provides the timing and phase noise PSDs for the generation of a f_c = 300 GHz signal via optical frequency generation with the contributions from Eq. (9). We note that for the 300-GHz signal, the timing (phase) noise is considerably lower than that of the time transfer itself for Fourier frequencies above this 1 Hz synchronization bandwidth. Based on the PSDs in Figs. 8(a) and 8(b), we generate the integrated phase noise curves in Fig. 7(b) and the Allan deviation in Fig. 9.

For good fringe visibility, one would like the rms phase fluctuations to be much less than 1 rad over the coherent integration time.[81] For a 300 GHz carrier, in Fig. 7(b), we can see that the integrated phase noise remains under 0.02 rad out to 1000 s—for context, the current Event Horizon Telescope has integration times on the order of 10 s.[71] We note that, in addition to the challenges of significant relative motion and higher link loss, extension to cislunar orbits or beyond would lead to increased integrated phase noise due to the reduction of the maximum synchronization bandwidth by ≈10×. However, at a 100 mHz synchronization bandwidth, the integrated phase noise would remain at ~0.1 rad for a 300 GHz carrier.

As the integrated phase noise in Fig. 7(b) is carrier frequency dependent, we can use the fractional frequency instability (ADEV) of the noise in Fig. 9 instead to project out performance beyond 300 GHz.[24] In this case, following Refs. 71 and 81, we can write an expression for the loss of coherence as $1 - e^{-(2\pi f_c T_{int}\sigma_y)^2}$, where T_{int} is the coherent integration time and σ_y is the Allan deviation. At T_{int} = 10 s, σ_y = 1.0×10^{-15}, and f_c = 300 GHz, the projected coherence loss is 0.03%, and even if f_c is increased to 1 THz, it only rises to 0.4%, which stands in contrast to the ~5% coherence loss expected for f_c = 230 GHz, T_{int} = 10 s, and a hydrogen maser reference at $\sigma_y(\tau = 10\text{ s}) = 1.5 \times 10^{-14}$.[71]

V. FUTURE WORK

Here, we have focused on the two specific applications of optical time transfer to geosynchronous orbit: intercontinental time transfer and coherence transfer. Several directions for the extension of this work exist.

The first is that the choice of ground-to-geosynchronous orbit links allowed us to put aside the consideration of relative platform motion. In order to consider expansion to ground-to-LEO, MEO, HEO, or cislunar links, the quantum-limited approach to optical time transfer considered here must be extended to track the high relative velocities and the associated acceleration and jerk. If a different orbit is chosen for either intercontinental time transfer or a coherence transfer system, both the effective holdover time or close loop phase correction transfer function and one-way time-of-flight will change, and, thus, the project performance will shift accordingly based on either Eqs. (7) or (8). In addition, the impact of turbulence and anisoplanatism must be included in any noise analysis.

The second is that, as noted above, we have not focused on the relativistic effect of time dilation. In considering an expansion beyond geosynchronous orbits, not only must the system be able to track the relative platform motion, but the relativistic corrections necessary will be considerable. In addition, as optical atomic clocks approach a higher TRL and become flight-capable, the relativistic effects on space-borne optical atomic clocks must be considered at the 1×10^{-19} level or even better for future tests of fundamental physics and other experiments. Fortunately, the outlook for this is promising, as there is already significant work focused on the impact of relativity with clocks in LEO with their extremely large relative velocities,[26,82] and the comparatively modest atomic clocks onboard the two eccentric Galileo satellites led to a groundbreaking gravitational redshift test.[83]

VI. CONCLUSION

In conclusion, we have presented a noise analysis of comb-based free-space optical time transfer to help predict the performance of future intercontinental time transfer via geostationary satellites and coherence transfer from the ground to a geosynchronous orbit satellite. In both cases, we find that a low-SWaP, miniaturized cavity-stabilized laser is sufficient for the space-based optical reference oscillator. In the case of the intercontinental time transfer, we find that we can reach a fractional frequency instability (MDEV) of 2×10^{-16} at 10-s averaging and maintain a time deviation less than 10 fs out to 10^5-s averaging. In the case of a coherence transfer system, we find that we support an integrated phase noise for 300 GHz generation of 10 mrad at 10-s averaging. This level of performance suggests that the use of quantum-limited optical time transfer over ground-to-geosynchronous-orbit links can support future fundamental tests and distribute coherent sensing out to THz carrier frequencies, among other wide-ranging applications.

AUTHOR DECLARATIONS

Conflict of Interest

The authors have no conflicts to disclose.

Author Contributions

Emily D. Caldwell: Conceptualization (equal); Formal analysis (equal); Visualization (equal); Writing – original draft (equal); Writing – review & editing (equal). **Laura C. Sinclair**: Conceptualization (equal); Formal analysis (equal); Visualization (equal); Writing – original draft (equal); Writing – review & editing (equal). **Jean-Daniel Deschenes**: Conceptualization (equal); Formal analysis (supporting); Visualization (supporting); Writing – review & editing (equal). **Fabrizio Giorgetta**: Formal analysis (supporting); Writing – original draft (supporting); Writing – review & editing (equal). **Nathan R. Newbury**: Conceptualization (equal); Formal analysis (supporting); Visualization (supporting); Writing – original draft (equal); Writing – review & editing (equal).

DATA AVAILABILITY

Data sharing is not applicable to this article as no new data were created or analyzed in this study.

APPENDIX A: KALMAN FILTER-BASED MODELING

We want to estimate the timing uncertainty on the comb pulse train during a holdover period due to the timing noise on the reference oscillator. At a high-level, this is done by modeling each fractional frequency noise component of the reference oscillator in state-space, seeding the Kalman filter with perfect initial timing knowledge (i.e., assuming previous high accuracy two-way time transfer measurements), repeating the prediction step of the Kalman filter without observation for each holdover time, and calculating the uncertainty in the timing. The following section describes how we model the oscillator noise in state-space and run the Kalman filter to provide an estimate of timing uncertainty.

We model the fractional frequency noise PSD of the reference oscillator (cavity stabilized laser) as

$$S_{y,cavity}(f) = h_{-2}f^{-2} + h_{-1}f^{-1} + h_0, \quad (A1)$$

where the terms are, in order, the random walk frequency noise (f^{-4} phase/timing noise), the flicker frequency noise (f^{-3} phase/timing noise), and the; white frequency noise (f^{-2} phase/timing noise). Because the Kalman filter will assume white process noise, we generate these noise sources through the filtering of white noise. Clearly, the white-frequency noise component is directly modeled without filtering. The random walk noise can be modeled by applying an integral filter, and far from the sampling frequency, f_s can be approximated with the transfer function $|H(f)|^2 = \frac{f_s^2}{4\pi^2 f^2}$. We generate the flicker noise through approximation by cascading single pole infinite impulse response (IIR) low pass filters. An example of this modeling is shown for the low-SWaP cavity stabilized laser in Fig. 10.

Ultimately, we are interested in timing uncertainty, so we begin by writing the state-space equation for the timing noise of the kth sample,
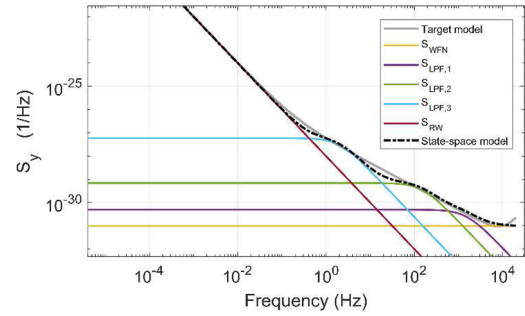

FIG. 10. State-space components to model low-SWaP cavity noise. The target model (gray) is approximated with white frequency noise (S_{WFN}, yellow), low pass filtered white noise (S_{LPF}, various colors), and random walk frequency noise (S_{RW}, red), which sum to the state-space model (dashed black).

$$X[k] = X[k-1] + TY_{LPF,1}[k-1] + TY_{LPF,2}[k-1]$$
$$+ TY_{LPF,3}[k-1] + TY_{RW}[k-1] + T\sigma_0 \nu_0[k-1], \quad (A2)$$

where $Y_{LPF,1}$ is the fractional frequency noise generated by low pass filtering white-noise with variance σ_1^2 with a cutoff frequency $f_{c,1}$ (the other low-pass filtered components follow), Y_{RW} is the random walk fractional frequency noise generated by integrating white noise, ν_0 is the Gaussian white noise with a variance of 1, and $\sigma_0^2 = S_{WFN}(f_s/2)$ is the set by the white frequency noise level S_{WFN}. All the fractional frequency components are integrated by multiplication with a time interval of $T = 1/f_s$ for conversion to timing fluctuations.

We can write similar state equations for each noise component. For the low-pass filtered noise, we can define $\alpha_1 = e^{-2\pi f_{c,1}/f_s}$ and $\beta_1 = 1 - \alpha_1$ to write

$$Y_{LPF,1}[k] = \alpha_1 Y_{LPF,1}[k-1] + \beta_1 \sigma_1 \nu_1[k-1], \quad (A3)$$

where ν_1 is the Gaussian white noise with a variance of 1, σ_1^2 is the set by the fractional frequency noise level of the desired low-pass filtered noise below the cutoff frequency, and $S_{LPF,1}(f < f_{c,1}) = 2\sigma_1^2/f_s$. Similarly, the random-walk frequency noise can be written as

$$Y_{RW} = Y_{RW}[k-1] + \sigma_4 \nu_4[k-1]. \quad (A4)$$

Here, the variance of the white noise is set by the value of the desired random walk noise at 1 Hz, $\sigma_4^2 = 2\pi^2 S_{RW}(1 \text{ Hz})/f_s$.

Combining Eqs. (A2)–(A4) and including copies of (A3) for each low pass filtered noise component, we can write a state vector,

$$\mathbf{x_k} = \begin{bmatrix} X[k] \\ Y_{LPF,1}[k] \\ Y_{LPF,2}[k] \\ Y_{LPF,3}[k] \\ Y_{RW}[k] \end{bmatrix} \quad (A5)$$

that progress according to $\mathbf{x_k} = \mathbf{Ax_{k-1}} + \mathbf{w_{k-1}}$, where the process noise vector, $\mathbf{w_{k-1}}$, is given as

$$\mathbf{w_k} = \begin{bmatrix} T\sigma_0\nu_0[k] \\ \beta_1\sigma_1\nu_1[k] \\ \beta_2\sigma_2\nu_2[k] \\ \beta_3\sigma_3\nu_3[k] \\ \sigma_4\nu_4[k] \end{bmatrix} \tag{A6}$$

and the state transition matrix $\mathbf{A}$ is written as

$$\mathbf{A} = \begin{bmatrix} 1 & T & T & T & T \\ 0 & \alpha_1 & 0 & 0 & 0 \\ 0 & 0 & \alpha_2 & 0 & 0 \\ 0 & 0 & 0 & \alpha_3 & 0 \\ 0 & 0 & 0 & 0 & 1 \end{bmatrix}. \tag{A7}$$

Notice there is no dedicated state for the white frequency noise; rather, it enters through the process noise in the timing noise state.

From $\mathbf{w_k}$, we can write the process covariance matrix,

$$\mathbf{Q} = \begin{bmatrix} T^2\sigma_0^2 & 0 & 0 & 0 & 0 \\ 0 & \beta_1^2\sigma_1^2 & 0 & 0 & 0 \\ 0 & 0 & \beta_2^2\sigma_2^2 & 0 & 0 \\ 0 & 0 & 0 & \beta_3^2\sigma_3^2 & 0 \\ 0 & 0 & 0 & 0 & \sigma_4^2 \end{bmatrix}. \tag{A8}$$

Using these vectors and matrices to construct a Kalman filter, we repeatedly run the prediction step for the timing $\mathbf{x_k} = \mathbf{Ax_{k-1}}$ and timing uncertainty $\mathbf{P_k} = \mathbf{AP_{k-1}A^T} + \mathbf{Q}$, where $\mathbf{P_k}$ is the state error covariance matrix. For simplicity, we initialize $\mathbf{P}$ as the null matrix, which is the same as assuming perfect knowledge of the pulse timing. $\mathbf{P_k}(1,1)$ gives us the timing uncertainty after k iterations of prediction, which can be directly mapped to holdover time.

APPENDIX B: MODIFIED ALLAN DEVIATION DUE TO REFERENCE OSCILLATOR NOISE AND DELAY

1. Derivation

Here, we derive the modified Allan deviation resulting from a delay t_h between two measurements due to noise on the local oscillator, i.e., the cavity stabilized laser. Its fractional frequency noise PSD is again given by (A1). The differential frequency noise PSD that corresponds to measurements delayed by t_h is

$$S_{y,dcavity}(f, t_h) = 4\sin^2(\pi f t_h)S_{y,cavity}. \tag{B1}$$

The corresponding modified Allan variation[25] is

$$MVAR(t_{avg}, t_h) = \int_0^\infty S_{y,dcavity}(f, t_h)|W_M(f, t_{avg})|^2 df, \tag{B2}$$

where the filter function is

$$|W_M(f, t)|^2 = \frac{2\sin^6(\pi f t)}{(\pi f t)^4}. \tag{B3}$$

The square root of Eq. (B2) gives the Modified Allan Deviation (MDEV) for the differential frequency noise and is shown in Fig. 4(c) as a function of t_h for $t_{avg} = 10$ s. Figure 2 gives the MDEVs for the unfiltered $S_{y,cavity}$ for the fractional frequency noise coefficients given in Table I.

2. Transfer function for differential measurements (H_{diff} derivation)

Consider a noise signal $x(t)$ with a delayed difference $y(t) = x(t) - x(t - t_0) = x(t) * [1 - \delta(t - t_0)]$.

Taking the Fourier transform of $y(t)$, where $F\{x(t)\} = \tilde{X}(f)$

$$F\{y(t)\} = \tilde{X}(f)[1 - e^{-i2\pi f t_0}]$$
$$= \tilde{X}(f)e^{-i\pi f t_0}[e^{i\pi f t_0} - e^{-i\pi f t_0}].$$

Defining $H_{diff}(t_0) = e^{-i\pi f t_0}[e^{i\pi f t_0} - e^{-i\pi f t_0}]$, we can write the squared magnitude response,

$$|H_{diff}|^2 = |e^{-i\pi f t_0}[e^{i\pi f t_0} - e^{-i\pi f t_0}]|^2$$
$$= 4\sin^2(\pi f t_0). \tag{B4}$$

The power spectral density of $y(t)$ is

$$S_y = |F\{y(t)\}|^2$$
$$= |\tilde{X}(f)|^2|H_{diff}|^2$$
$$= |\tilde{X}(f)|^2 4\sin^2(\pi f t_0).$$

APPENDIX C: NOISE ANALYSIS

1. General

This section derives Eqs. (7) and (8), which describe the contribution of the various noise sources described in Sec. II to the total noise on intercontinental clock comparison and coherence transfer. While the ultimate output of either case is a time offset, it can be useful to think in units of clock phase, assuming a consistent underlying frequency of f_r at each site. In other words, we convert the time at site A as $\varphi_A = 2\pi f_r \tau_A$ and site X as $\varphi_X = 2\pi f_r \tau_X$. Two phase differences are measured across the XA two-way link: the relative phase of the pulses launched from site A and measured at site X, $\delta\varphi_{A \to X}$, and the relative phase of the site X pulses measured at site A, $\delta\varphi_{X \to A}$. These are

$$\delta\varphi_{A \to X}(t) = \varphi_A(t - TOF_{AX}) - \varphi_{turb}(t - TOF_{AX}) - \varphi_X(t),$$
$$\delta\varphi_{X \to A}(t) = \varphi_X(t - TOF_{AX}) - \varphi_{turb}(t) - \varphi_A(t), \tag{C1}$$

both assume to be measured at some common time t to within ~1 ns accuracy given by a coarser time transfer (e.g., GNSS system). For now, we assume a static time-of-flight, TOF_{AX}, between the two sites. We separate out the time-of-flight variations due to turbulence, φ_{turb}, which appear in the second term of each equation. For the turbulence, we use a simple lumped model in which the turbulence is located very near the ground (i.e., site A), so the pulse train departing site A encounters it immediately, while the pulse train from site X to

site A encounters it just before reaching site A. (We ignore the very small time-of-flight between the effective center of the turbulence layer and the ground.)

Practically speaking, $\delta\varphi_{A \to X}$ is measured at site X by replicating $\varphi_A(t - TOF_{AX})$ (the incoming clock comb phase) with the tracking LO comb phase, which itself is measured against the local clock comb phase φ_X. $\delta\varphi_{A \to X}$ is measured with respect to the site X reference oscillator, so the conversion to time will depend on the repetition frequency of the comb at site X, $f_{rX}(t)$. The difference between this repetition frequency and that of the comb at site A is captured later by the phase noise term of the site X reference oscillator.

In the limit of $TOF_{AX} = 0$, the difference of these two one-way phase measurements yields the phase (time) difference between our two oscillators, $\Delta\varphi_{AX}$,

$$\frac{\delta\varphi_{A \to X}(t) - \delta\varphi_{X \to A}(t)}{2} = \varphi_A(t) - \varphi_X(t) \equiv \Delta\varphi_{AX}, \quad \text{(C2)}$$

independent of the turbulence-induced phase noise. For the coherence transfer, this is the phase offset of interest. For the intercontinental clock comparison, analogous phases for the BX link are similarly combined to yield the ultimate clock phase comparison, $\Delta\varphi_{AB}$.

A first order Taylor expansion for each phase returns,

$$\varphi_A(t - TOF_{A \to X}(t)) \approx \varphi_A(t) - 2\pi f_r TOF_{A \to X}(t), \quad \text{(C5)}$$

$$\varphi_x(t - TOF_{X \to A}(t)) \approx \varphi_x(t) - 2\pi f_r TOF_{X \to A}(t), \quad \text{(C6)}$$

where we have assumed the time derivatives of φ_A and φ_X are set by the repetition rate, that is, $\delta\dot\varphi_x = \delta\dot\varphi_A = 2\pi f_r$.

Substituting Eqs. (C5) and (C6) into Eq. (C4) yields

$$\frac{\delta\varphi_{A \to X}(t) - \delta\varphi_{X \to A}(t)}{2}$$
$$\approx \Delta\varphi_{AX} + \pi f_r [TOF_{X \to A}(t) - TOF_{A \to X}(t)]. \quad \text{(C7)}$$

Assuming site X is moving with a constant velocity $V(t)$, where a positive velocity corresponds to an increasing time-of-flight, from Fig. 5, we can see that $TOF_{X \to A} < TOF_{A \to X}$ and

$$TOF_{X \to A}(t) - TOF_{A \to X}(t) \approx \frac{V \times TOF_{X \to A}}{c}. \quad \text{(C8)}$$

Substituting this into Eq. (C7) gives our final result,

$$\frac{\delta\varphi_{A \to X}(t) - \delta\varphi_{X \to A}(t)}{2} \approx \Delta\varphi_{AX} + \pi f_r \frac{V}{c} TOF_{X \to A}(t). \quad \text{(C9)}$$

2. Non-reciprocal time-of-flight due to platform motion

While the radial velocity of a GEO satellite is orders of magnitude smaller than MEO or LEO, site X on the satellite will still move on the order of ~1 m/s at points during a month-long window due to station keeping and will see additional movement due to vibrations.[84] This motion will cause a breakdown in the time-of-flight reciprocity for a two-way link if pulses from each site leave simultaneously. Here, we discuss the consequences of a non-reciprocal time-of-flight.

We expand the previous discussion to allow for time-varying and non-reciprocal time-of-flights for pulses traveling from site A to X, $TOF_{A \to X}(t)$, and from site X to A, $TOF_{X \to A}(t)$. The phases measured at the two sites follow from Eq. (C1),

$$\delta\varphi_{A \to X}(t) = \varphi_A(t - TOF_{A \to X}(t)) - \varphi_{turb}(t - TOF_{A \to X}(t)) - \varphi_X(t),$$
$$\delta\varphi_{X \to A}(t) = \varphi_X(t - TOF_{X \to A}(t)) - \varphi_{turb}(t) - \varphi_A(t), \quad \text{(C3)}$$

where the time-of-flight, $TOF_{A \to X}(t)$, is defined as the duration for a pulse to travel from site A to site X with an arrival time at site X of t. To isolate the effect of motion, we will set $\varphi_{turb} = 0$, although it is important to note that turbulence-induced time-of-flight variations (piston noise) and platform motion are indistinguishable within the signal, and we will address this later. Taking the difference between the two phases yields

$$\frac{\delta\varphi_{A \to X}(t) - \delta\varphi_{X \to A}(t)}{2} = \frac{\varphi_A(t - TOF_{A \to X}(t)) + \varphi_A(t) - \varphi_X(t) - \varphi_X(t - TOF_{X \to A}(t))}{2}. \quad \text{(C4)}$$

Here, for $V = 1$ m/s and $TOF_{X \to A} = 120$ ms, the velocity-dependent term would introduce an error of 200 ps into $\Delta\varphi_{AX}$. Thus, a velocity correction based on the measured instantaneous velocity must be applied to the $\Delta\varphi_{AX}$, as has already been demonstrated in Refs. 7 and 8, for up to 25 m/s. In Ref. 8, the velocity was estimated to be within 20μm/s at one-second averaging—a similar modest effort at estimating the velocity would allow us here to reduce the velocity-dependent error to 4 fs. A lower bound for the velocity-dependent error can be estimated to be ≈ 1 fs at one-second averaging from the ADEV in Fig. 9, as instantaneous velocity is estimated from the sum of the phases (time-of-flight measurements), which shares the instability of the difference of the phases (time offset measurements).

We note that a 1-Hz update rate (1-second averaging time) for the velocity estimate is reasonable for not only post-processing but also real-time synchronization with $TOF \approx 120$ ms given the relatively low velocities and accelerations of a GEO orbit. For the cases of LEO, MEO, or cis-lunar orbits, the velocity-dependent errors post-correction will be complicated by the high acceleration and jerk, and additional care will need to be taken in applying delays and correction terms.

3. Intercontinental clock comparison

Here, we derive the noise on the clock comparison, $\Delta\varphi_{AB}$. The various contributing signals and noise sources are outlined in Fig. 11.
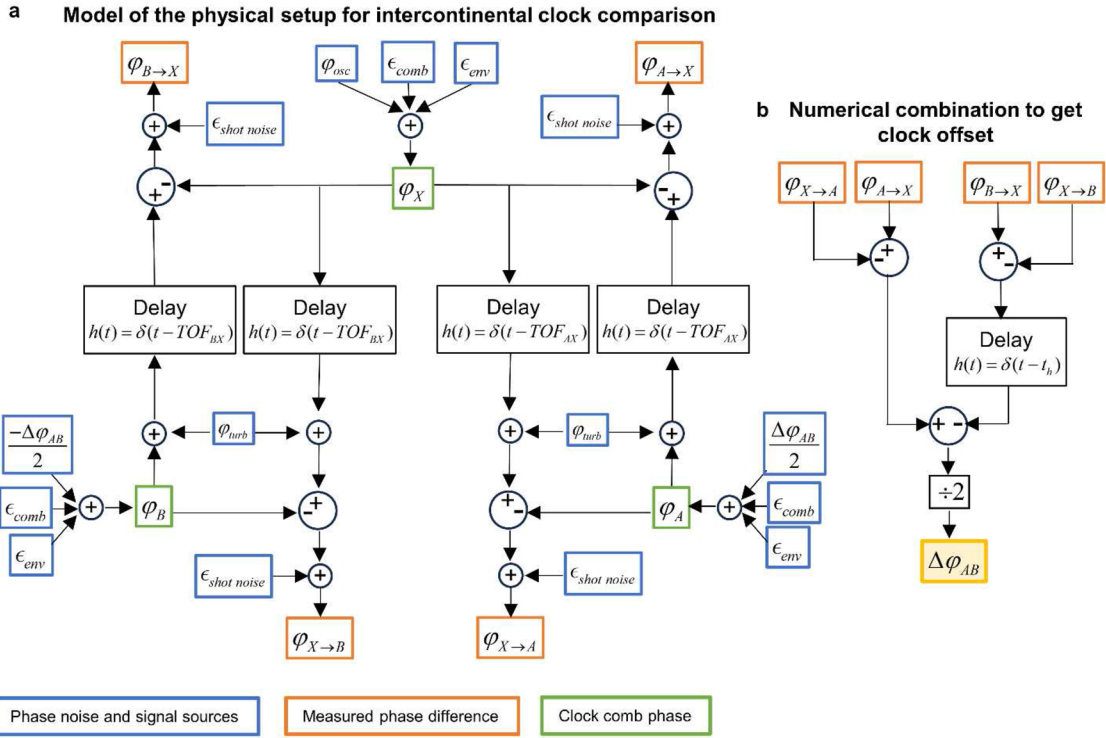
FIG. 11. Noise flow chart in intercontinental time transfer. (a) Chart outlining both the phase signals and associated noise sources (blue boxes) that contribute to each clock comb phase (green boxes) and the measurements of the phase difference at each site (orange boxes). The phases are all referenced to an assumed common reference frequency of f_r, as described in the text. (b) The linear combination of the measured phase differences yields the final clock offset phase $\Delta\varphi_{AB}$.

First, we consider the simplest case of noise caused by a holdover time, t_h, which derives from Eq. (1) in the main text. We then consider the remaining noise sources.

The analogous equations to Eq. (C1) for the BX link are

$$
\begin{aligned}
\delta\varphi_{B\to X}(t - t_h) &= \varphi_B(t - TOF_{BX} - t_h) \\
&\quad - \varphi_{turbBX}(t - TOF_{BX} - t_h) - \varphi_X(t - t_h), \\
\delta\varphi_{X\to B}(t - t_h) &= \varphi_X(t - TOF_{BX} - t_h) \\
&\quad - \varphi_{turbBX}(t - t_h) - \varphi_B(t - t_h),
\end{aligned} \tag{C10}
$$

where the delay t_h indicates the measurements on the *BX* link are taken at a different time than the *AX* link, assuming asynchronous operation. The ultimate output of the clock comparison is $\Delta\varphi_{AB}$, which in the limit of all $TOF_{A(B)X} = 0$ and $t_h = 0$, is

$$
\begin{aligned}
\left(\frac{\delta\varphi_{A\to X} - \delta\varphi_{X\to A}}{2}\right) &- \left(\frac{\delta\varphi_{B\to X} - \delta\varphi_{X\to B}}{2}\right) \\
&= \Delta\varphi_{AX} - \Delta\varphi_{BX} \equiv \Delta\varphi_{AB}.
\end{aligned} \tag{C11}
$$

If we relax these assumptions to allow for a non-zero t_h delay between the measurements,

$$
\begin{aligned}
\left(\frac{\delta\varphi_{A\to X} - \delta\varphi_{X\to A}}{2}\right) &- \left(\frac{\delta\varphi_{B\to X} - \delta\varphi_{X\to B}}{2}\right) \\
&= \varphi_A(t) - \varphi_B(t - t_h) + \varphi_X(t - t_h) - \varphi_X(t).
\end{aligned} \tag{C12}
$$

In the text, we assumed that the ground clocks are much more stable than the space oscillator. Here, we apply this assumption by asserting that φ_B is stable enough that $\varphi_B(t) \approx \varphi_B(t - \Delta t_B)$, which yields

$$
\begin{aligned}
\left(\frac{\delta\varphi_{A\to X} - \delta\varphi_{X\to A}}{2}\right) &- \left(\frac{\delta\varphi_{B\to X} - \delta\varphi_{X\to B}}{2}\right) \\
&= \Delta\varphi_{AB} - \delta\varphi_X(t_h),
\end{aligned} \tag{C13}
$$

where $\delta\varphi_X(t_h) = \varphi_X(t - t_h) - \varphi_X(t)$ is the differential phase noise of the oscillator. Converting this back to time gives us Eq. (1) in the holdover discussion of the main text.

To consider other noise sources, we return to Eq. (C12) and assume non-zero time-of-flight, $TOF_{A(B)X}$, as well as the additional noise sources in Fig. 11. In addition, we recognize that there might be a desired time offset, Δt, between the comparison of the two two-way *AX* and *BX* measurements in addition to any varying and uncontrolled holdover time, t_h. The linear combination of Eq. (C1), Eq. (C10) with $t_h \to t_h + \Delta t$, and Eq. (C12) gives

$$\frac{1}{2}\left(\delta\varphi_{A\to X} - \delta\varphi_{X\to A} - \delta\varphi_{B\to X} + \delta\varphi_{X\to B}\right) = \frac{1}{2}\big(\varphi_A(t - TOF_{AX}) + \varphi_A(t) - \varphi_B(t - TOF_{BX} - t_h - \Delta t) - \varphi_B(t - t_h - \Delta t)$$
$$+ \varphi_X(t - t_h - \Delta t) + \varphi_X(t - TOF_{BX} - t_h - \Delta t) - \varphi_X(t) - \varphi_X(t - TOF_{AX})$$
$$- \varphi_{turbAX}(t - TOF_{AX}) + \varphi_{turbAX}(t) - \varphi_{turbBX}(t - t_h - \Delta t)$$
$$+ \varphi_{turbBX}(t - TOF_{BX} - t_h - \Delta t)\big), \tag{C14}$$

where each phase includes both a signal and added noise components as

$$\varphi_A(t) = \frac{\Delta\varphi_{AB}(t)}{2} + \boldsymbol{\epsilon}_{comb}(t) + \boldsymbol{\epsilon}_{env}(t),$$
$$\varphi_B(t) = -\frac{\Delta\varphi_{AB}(t)}{2} + \boldsymbol{\epsilon}_{comb}(t) + \boldsymbol{\epsilon}_{env}(t),$$
$$\varphi_X(t) = \Delta\varphi_{osc} + \boldsymbol{\epsilon}_{comb}(t) + \boldsymbol{\epsilon}_{env}(t), \tag{C15}$$
$$\varphi_{turbAX}(t) = \boldsymbol{\epsilon}_{turb}(t),$$
$$\varphi_{turbBX}(t) = \boldsymbol{\epsilon}_{turb}(t),$$

where we drop the common assumed $2\pi f_r t$ progression of all three phases, $\varphi_{A(B)(X)}(t)$. We write the offset in the phase at sites A and B in terms of their difference, $\Delta\varphi_{AB}$, assuming a reference frequency of f_r. At site X, $\Delta\varphi_{osc}$ is the phase noise of the reference oscillator scaled from its nominal optical reference frequency to f_r. The terms ϵ are additional phase noise (ϵ_{comb}: residual comb noise, ϵ_{env}: environmental noise, ϵ_{turb}: turbulence piston noise, which we assume has equal magnitude on both links). Note that while the time series realizations of each noise term differ between the three phases, that is, $\epsilon_{env}(t)$ contributing to $\varphi_A(t)$ is different than $\epsilon_{env}(t)$ contributing to $\varphi_B(t)$, we have written them with the same symbols since they share common PSDs and to simplify the notation. Since all combs are running at a nominal f_r, we can convert each of these phases to time offsets as $\tau = \varphi/(2\pi f_r)$, where $\Delta\tau_{AB} = 2\pi f_r \Delta\varphi_{AB}$ is the final timing comparison of interest. We can then write the timing jitter PSD of each clock comb phase,

$$S_{\tau A} = S_{comb} + S_{env},$$
$$S_{\tau B} = S_{comb} + S_{env}, \tag{C16}$$
$$S_{\tau X} = S_{osc} + S_{comb} + S_{env},$$

and S_{turb} is the turbulence-induced timing noise. Note that there is no explicit shot noise contribution since it arises in the actual measurements of $\varphi_{A\to X}$, $\varphi_{X\to A}$, $\varphi_{B\to X}$, and $\varphi_{X\to B}$ and is, therefore, included later in the combined two-way equation. Combining Eq. (C14) and the noise terms from Eqs. (C15) and (C16) and converting to timing noise, we can write the noise on $\Delta\tau_{AB}$ as

$$S_{\Delta\tau AB} = \frac{1}{4}\big(4S_{comb} + 4S_{env} + 2|H_{diff}(t_h)|^2(S_{osc} + S_{comb} + S_{env})$$
$$+ 2|H_{diff}(TOF)|^2 S_{turb} + 4S_{sn}\big). \tag{C17}$$

Here, the first two terms assume the optical clocks at sites A and B are significantly more stable than the oscillator at site X, meaning any differential delay noise from the subtraction of the φ_A and φ_B terms in Eq. (C14) can be ignored. The third term comes from

the differences between the different delayed φ_X terms, which are minimized by setting,

$$\Delta t = \frac{TOF_{AX} - TOF_{BX}}{2}, \tag{C18}$$

leaving t_h as the dominant delay. The quantity $|H_{diff}(t_{delay})|^2 = 4\sin^2(\pi f t_{delay})$ is the differential delay transfer function derived in Appendix B 2. The fourth term comes from assuming the same turbulence noise on each link and letting $TOF_{AX} \approx TOF_{BX} = TOF$. The last term comes from assuming the same shot noise S_{sn} on each measurement of $\varphi_{A\to X}$, $\varphi_{X\to A}$, $\varphi_{B\to X}$, and $\varphi_{X\to B}$ based on the use of the optical timing discriminator in Ref. 64 and assuming in all cases a minimal 270 fW of received power. Again, here we assume there is some uncertainty in how well we can realize (C18), which is captured by t_h, and which dominates any second order noise terms in the Taylor expansion of the φ_X terms in Eq. (C14).

We can further simplify Eq. (C17) by recognizing that $\langle|H_{diff}(t_h)|^2\rangle \approx 2$ for $f > 1/(2t_h)$. If we assume t_h is order 1 ms (cutoff frequency of 500 Hz), then the PSD of $S_{\tau X}$ will simply be doubled beyond this frequency. Since S_{osc} is greater than S_{env} and S_{comb} until ~ 1 kHz, we can approximate the third term in (C17) by doubling S_{env} and S_{comb} and applying H_{diff} to S_{osc} only (see Fig. 12).

This approximation yields Eq. (7) of the text,

$$S_{\Delta\tau AB} = 2S_{comb} + 2S_{env} + S_{sn} + \frac{1}{2}|H_{diff}(t_h)|^2(S_{osc})$$
$$+ \frac{1}{2}|H_{diff}(TOF)|^2 S_{turb}. \tag{C19}$$

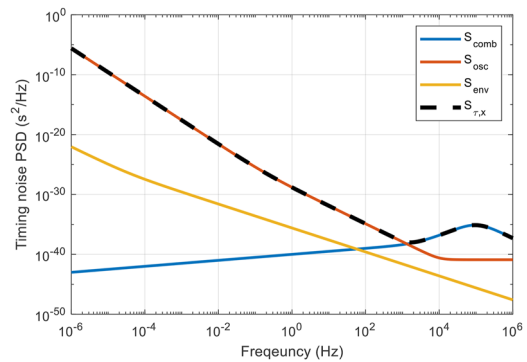**FIG. 12.** Components of $S_{\tau_x} = S_{osc} + S_{comb} + S_{env}$. Notice S_{τ_x} will follow S_{osc} at low frequencies up to ~ 1 kHz, after which it will be dominated by residual frequency comb noise S_{comb}.

4. Coherence transfer system

First, we derive the noise from the measured time/phase offset between the ground oscillator and space-based oscillator, $\Delta\tau_{AX}$. A chart of the phase combinations needed for each measurement, along with the noise contributions, is shown in Fig. 13. In contrast to the intercontinental time transfer case, here $\Delta\tau_{AX}$, or the equivalent scaled phase difference $\Delta\varphi_{AX}$, will be used to apply a phase correction to the space-based oscillator either in real-time or in post-processing. The phases measured on sites A and X are given by Eq. (C1), except that here we set $\Delta\varphi_{osc} \equiv 0$ since our objective is to measure this quantity. In the absence of the noise terms and at zero time-of-flight, we have, as before,

$$\Delta\varphi_{AX}(t) = \frac{\delta\varphi_{A\rightarrow X} - \delta\varphi_{X\rightarrow A}}{2}. \qquad (C20)$$

As before, we can convert these phases to time with $\tau_{AX} = \Delta\varphi_{AX}/(2\pi f_r)$. The noise in this measurement arises from similar noise contributions as in Eq. (C15) and the shot-noise associated with the optical timing discriminator. The corresponding timing PSDs for the noise in this OTT measurement is

$$S_{\Delta\tau AX} = S_{comb} + S_{env} + \frac{1}{2}S_{sn} + \frac{1}{4}|H_{diff}(TOF)|^2 S_{turb} \qquad (C21)$$

or Eq. (8) in the main text.

At low Fourier frequencies, this OTT noise will lie below the free-running reference oscillator noise, and we should implement a closed loop phase correction to reduce the free-running oscillator noise (i.e., synchronize the sites). At higher Fourier frequencies, the free running reference oscillator will provide lower phase noise. The crossover is set by the bandwidth of the closed loop phase correction transfer function, H_{corr}. In Sec. IV B, we modeled H_{corr} as a two-pole low pass filter, which is similar to the synchronization transfer function actually implemented in Ref. 15. With this closed loop phase correction, the phase noise on the detected microwave signal follows the OTT results for low Fourier frequencies and the reference oscillator for high Fourier frequencies. In addition, there is added noise from the phase lock of the clock comb to the reference oscillator and from the photodetection process (including shot noise). The resulting microwave timing noise is

$$S_{\mu wave} = |H_{corr}|^2 S_{\Delta\tau AX} + |1 - H_{corr}|^2 (S_{osc} + S_{comb})$$
$$+ S_{photodetection} \qquad (C22)$$

or Eq. (9) in the main text.

If we implement real-time synchronization, then the maximum cutoff frequency will be set by the time-of-flight for stability to $f_c < (8TOF)^{-1} \approx 1$ Hz. This is the limit used in the simulations for Fig. 8, with the second integrator frequency set to $f_{c2} = \frac{1}{4}f_c$.
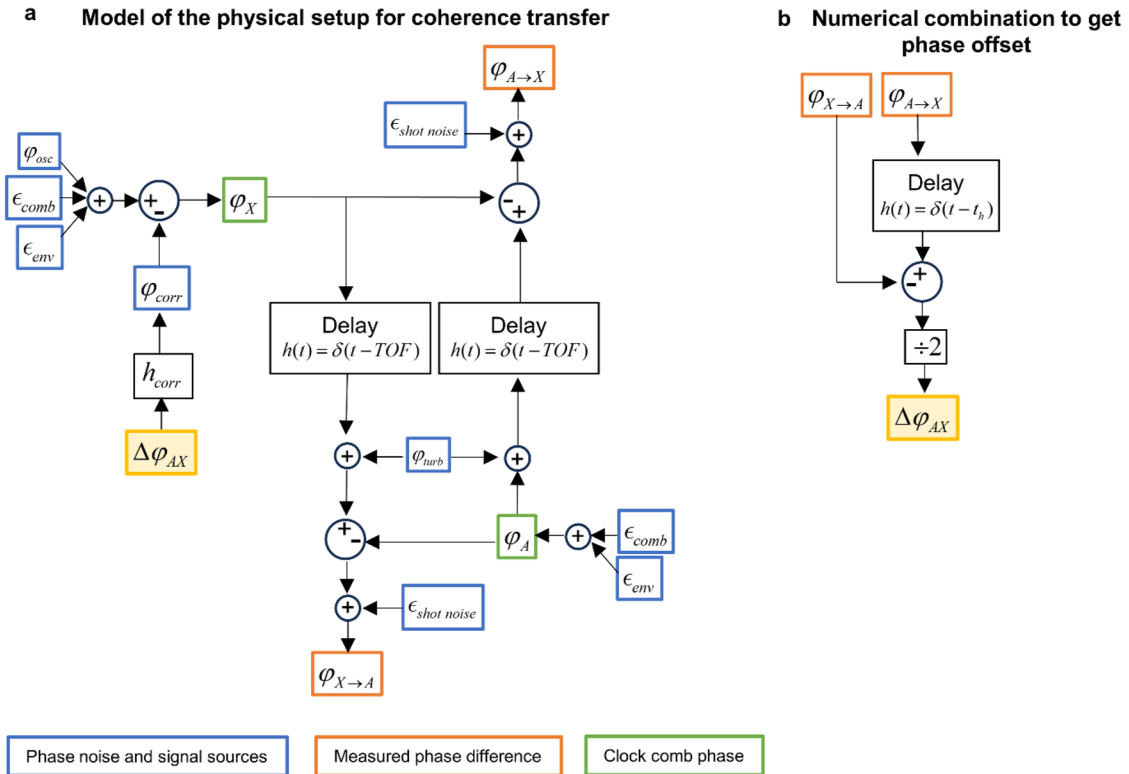

FIG. 13. Noise schematic for coherence transfer. (a) Chart showing the contributing noise sources and phases (blue boxes) to each clock comb phase (green boxes) and the measurements of the relative phases at each site (orange boxes). (b) The linear combination of the phase measurements to retrieve the relative phase offset between the two sites is subsequently used for the phase correction.
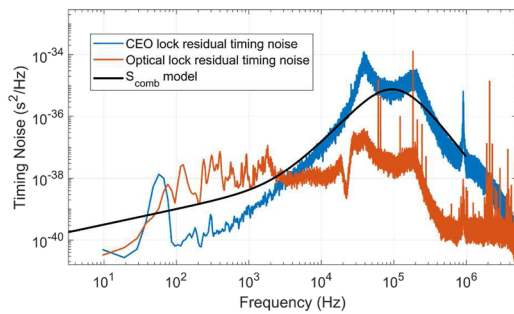
FIG. 14. Noise model for total residual comb noise (black) along with measured comb noise (red and blue). The CEO lock on this comb had 2.2 rad rms of phase noise.

If we implement a post-processed correction, this effective bandwidth could be higher. Interestingly, Fig. 8 shows the intersection between $\frac{1}{4}|H_{diff}(TOF)|^2 S_{turb}$ and S_{osc} is ~1.5 Hz, so it does not appear much bandwidth can be gained by doing this correction in post-processing.

5. Measured vs modeled comb noise

The comb noise discussed in the text is defined as the residual noise on a single frequency comb locked with both a 1f-2f carrier envelope offset (CEO) lock and a lock to an optical oscillator (optical) lock. The simple model for the comb noise given in the text is

$$S_{comb} = \left\{ \begin{array}{ll} 10^{-45} f^2 + 10^{-40} f^{1/2} & f < 10^5 \\ 5 \times 10^{-20} f^{-3} & f > 10^5 \end{array} \right\} \quad (s^2/Hz). \quad (C23)$$

This model is compared to the measured comb noise in Fig. 14.

REFERENCES

[1] F. R. Giorgetta, W. C. Swann, L. C. Sinclair, E. Baumann, I. Coddington, and N. R. Newbury, "Optical two-way time and frequency transfer over free space," Nat. Photonics 7(6), 434–438 (2013).

[2] J.-D. Deschênes, L. C. Sinclair, F. R. Giorgetta, W. C. Swann, E. Baumann, H. Bergeron, M. Cermak, I. Coddington, and N. R. Newbury, "Synchronization of distant optical clocks at the femtosecond level," Phys. Rev. X 6(2), 021016 (2016).

[3] L. C. Sinclair et al., "Synchronization of clocks through 12 km of strongly turbulent air over a city," Appl. Phys. Lett. 109(15), 151104 (2016).

[4] J. L. Ellis, M. I. Bodine, W. C. Swann, S. A. Stevenson, E. D. Caldwell, L. C. Sinclair, N. R. Newbury, and J.-D. Deschênes, "Scaling up frequency-comb-based optical time transfer to long terrestrial distances," Phys. Rev. Appl. 15(3), 034002 (2021).

[5] M. I. Bodine, J. L. Ellis, W. C. Swann, S. A. Stevenson, J.-D. Deschênes, E. D. Hannah, P. Manurkar, N. R. Newbury, and L. C. Sinclair, "Optical time-frequency transfer across a free-space, three-node network," APL Photonics 5(7), 076113 (2020).

[6] Q. Shen et al., "Free-space dissemination of time and frequency with 10^{-19} instability over 113 km," Nature 610, 661–666 (2022).

[7] H. Bergeron, L. C. Sinclair, W. C. Swann, I. Khader, K. C. Cossel, M. Cermak, J.-D. Deschênes, and N. R. Newbury, "Femtosecond time synchronization of optical clocks off of a flying quadcopter," Nat. Commun. 10(1), 1819 (2019).

[8] L. C. Sinclair, H. Bergeron, W. C. Swann, I. Khader, K. C. Cossel, M. Cermak, N. R. Newbury, and J.-D. Deschênes, "Femtosecond optical two-way time-frequency transfer in the presence of motion," Phys. Rev. A 99(2), 023844 (2019).

[9] W. C. Swann, M. I. Bodine, I. Khader, J.-D. Deschênes, E. Baumann, L. C. Sinclair, and N. R. Newbury, "Measurement of the impact of turbulence anisoplanatism on precision free-space optical time transfer," Phys. Rev. A 99(2), 023855 (2019).

[10] C. Robert, J.-M. Conan, and P. Wolf, "Impact of turbulence on high-precision ground-satellite frequency transfer with two-way coherent optical links," Phys. Rev. A 93(3), 033860 (2016).

[11] A. Belmonte, M. T. Taylor, L. Hollberg, and J. M. Kahn, "Effect of atmospheric anisoplanatism on earth-to-satellite time transfer over laser communication links," Opt. Express 25(14), 15676–15686 (2017).

[12] M. T. Taylor, A. Belmonte, L. Hollberg, and J. M. Kahn, "Effect of atmospheric turbulence on timing instability for partially reciprocal two-way optical time transfer links," Phys. Rev. A 101(3), 033843 (2020).

[13] B. K. Stuhl, "Atmospheric refraction corrections in ground-to-satellite optical time transfer," Opt. Express 29(9), 13706 (2021).

[14] L. Wang, W. Jiao, L. Hu, J. Chen, and G. Wu, "Residual timing jitter in the free-space optical two-way time and frequency transfer caused by atmospheric turbulence," Opt. Laser Technol. 163, 109365 (2023).

[15] E. D. Caldwell, J.-D. Deschenes, J. Ellis, W. C. Swann, B. K. Stuhl, H. Bergeron, N. R. Newbury, and L. C. Sinclair, "Quantum-limited optical time transfer for future geosynchronous links," Nature 618(7966), 721–726 (2023).

[16] P. Kurczynski et al., in Space Telescopes and Instrumentation 2022: Optical, Infrared, and Millimeter Wave (SPIE, 2022), pp. 215–224.

[17] K. Abich et al., "In-orbit performance of the GRACE follow-on laser ranging interferometer," Phys. Rev. Lett. 123(3), 031101 (2019).

[18] M. L. Kelleher, C. A. McLemore, D. Lee, J. Davila-Rodriguez, S. A. Diddams, and F. Quinlan, "Compact, portable, thermal-noise-limited optical cavity with low acceleration sensitivity," Opt. Express 31(7), 11954–11965 (2023).

[19] Vectron, "Ultra low noise oven controlled crystal oscillator," OX-175 datasheet, 2019.

[20] Disclaimer, "The use of tradenames in this manuscript is necessary to specify experimental results and does not imply endorsement by the National Institute of Standards and Technology."

[21] D. R. Gozzard, L. A. Howard, B. P. Dix-Matthews, S. F. E. Karpathakis, C. T. Gravestock, and S. W. Schediwy, "Ultrastable free-space laser links for a global network of optical atomic clocks," Phys. Rev. Lett. 128(2), 020801 (2022).

[22] B. P. Dix-Matthews, D. R. Gozzard, S. M. Walsh, A. S. McCann, S. F. E. Karpathakis, A. M. Frost, C. T. Gravestock, and S. W. Schediwy, "Towards optical frequency geopotential difference measurements via a flying drone," Opt. Express 31(9), 15075–15088 (2023).

[23] Q. Shen et al., "Experimental simulation of time and frequency transfer via an optical satellite–ground link at 10^{-18} instability," Optica 8(4), 471–476 (2021).

[24] E. Rubiola and F. Vernotte, "The companion of Enrico's chart for phase noise and two-sample variances," IEEE Trans. Microwave Theory Tech. 71, 2996–3025 (2023).

[25] S. T. Dawkins, J. J. McFerran, and A. N. Luiten, "Considerations on the measurement of the stability of oscillators with frequency counters," IEEE Trans. Ultrason., Ferroelectr. Freq. Control 54(5), 918–925 (2007).

[26] L. Blanchet, C. Salomon, P. Teyssandier, and P. Wolf, "Relativistic theory for time and frequency transfer to order c^{-3}," Astron. Astrophys. 370(1), 320–329 (2001).

[27] B. Bachman et al., "Flight phasemeter on the laser ranging interferometer on the GRACE follow-on mission," J. Phys.: Conf. Ser. 840(1), 012011 (2017).

[28] W. M. Folkner et al., "Laser frequency stabilization for GRACE-II," in Earth Science Technology Forum, Arlington, VA (JPL-NASA, 2010).

[29] J. Davila-Rodriguez, F. N. Baynes, A. D. Ludlow, T. M. Fortier, H. Leopardi, S. A. Diddams, and F. Quinlan, "Compact, thermal-noise-limited reference cavity for ultra-low-noise microwave generation," Opt. Lett. 42(7), 1277–1280 (2017).

[30] K. Numata, A. Yu, H. Jiao, S. Merritt, F. Micalizzi, M. Fahey, J. Camp, and M. Krainak, in International Conference on Space Optics — ICSO 2018 (SPIE, 2019), pp. 152–159.

[31] T. Schuldt et al., "Optical clock technologies for global navigation satellite systems," GPS Solutions 25(3), 83 (2021).

[32] K. W. Martin, G. Phelps, N. D. Lemke, M. S. Bigelow, B. Stuhl, M. Wojcik, M. Holt, I. Coddington, M. W. Bishop, and J. H. Burke, "Compact optical atomic clock based on a two-photon transition in rubidium," Phys. Rev. Appl. 9(1), 014019 (2018).

[33] C. Perrella, P. S. Light, J. D. Anstie, F. N. Baynes, F. Benabid, and A. N. Luiten, "Two-color rubidium fiber frequency standard," Opt. Lett. 38(12), 2122–2124 (2013).

[34] T. D. Schmidt et al., "COMPASSO: In-orbit verification of optical key technologies for future GNSS," in Proceedings of the 53rd Annual Precise Time and Time Interval Systems and Applications Meeting (ION-PTTI, 2022) pp. 158–182.

[35] M. Schioppo et al., "Comparing ultrastable lasers at 7 × 10⁻¹⁷ fractional frequency instability through a 2220 km optical fibre network," Nat. Commun. 13(1), 212 (2022).

[36] EUMETSAT Meteosat cloud mask MSG 0 degree.

[37] NOAA GOES-R Binary Cloud Mask.

[38] Boulder Atomic Clock Optical Network (BACON) Collaboration, "Frequency ratio measurements at 18-digit accuracy using an optical clock network," Nature 591, 564–569 (2021).

[39] W. F. McGrew et al., "Atomic clock performance enabling geodesy below the centimetre level," Nature 564(7734), 87 (2018).

[40] E. Oelker et al., "Optical clock intercomparison with 6 × 10⁻¹⁹ precision in one hour," Nat. Photonics 13, 714 (2019).

[41] M. Takamoto, Y. Tanaka, and H. Katori, "A perspective on the future of transportable optical lattice clocks," Appl. Phys. Lett. 120(14), 140502 (2022).

[42] L. C. Andrews, R. L. Phillips, and C. Y. Hopen, Laser Beam Scintillation with Applications (SPIE Press, Bellingham, WA, 2001).

[43] E. D. Caldwell et al., "Optical timing jitter due to atmospheric turbulence: Comparison of frequency comb measurements to predictions from micrometeorological sensors," Opt. Express 28(18), 26661–26675 (2020).

[44] J. M. Conan, G. Rousset, and P.-Y. Madec, "Wave-front temporal spectra in high-resolution imaging through turbulence," J. Opt. Soc. Am. A 12(7), 1559–1570 (1995).

[45] S. Bize, "The unit of time: Present and future directions," C. R. Phys. 20(1–2), 153–168 (2019).

[46] F. Riehle, "Optical atomic clocks could redefine unit of time," Physics 5, 126 (2012).

[47] F. Riehle, "Optical clock networks," Nat. Photonics 11(1), 25–31 (2017).

[48] M. S. Safronova, D. Budker, D. DeMille, D. F. J. Kimball, A. Derevianko, and C. W. Clark, "Search for new physics with atoms and molecules," Rev. Mod. Phys. 90(2), 025008 (2018).

[49] T. E. Mehlstäubler, G. Grosche, C. Lisdat, P. O. Schmidt, and H. Denker, "Atomic clocks for geodesy," Rep. Prog. Phys. 81(6), 064401 (2018).

[50] A. Derevianko and M. Pospelov, "Hunting for topological dark matter with atomic clocks," Nat. Phys. 10(12), 933–936 (2014).

[51] A. Hees, J. Guéna, M. Abgrall, S. Bize, and P. Wolf, "Searching for an oscillating massive scalar field as a dark matter candidate using atomic hyperfine frequency comparisons," Phys. Rev. Lett. 117(6), 061301 (2016).

[52] P. Wcisło et al., "New bounds on dark matter coupling from a global network of optical atomic clocks," Sci. Adv. 4(12), eaau4869 (2018).

[53] C. Sanner, N. Huntemann, R. Lange, C. Tamm, E. Peik, M. S. Safronova, and S. G. Porsev, "Optical clock comparison for Lorentz symmetry testing," Nature 567(7747), 204 (2019).

[54] R. Lange, N. Huntemann, J. M. Rahm, C. Sanner, H. Shao, B. Lipphardt, C.. Tamm, S. Weyers, and E. Peik, "Improved limits for violations of local position invariance from atomic clock comparisons," Phys. Rev. Lett. 126(1), 011102 (2021).

[55] B. M. Roberts et al., "Search for transient variations of the fine structure constant and dark matter using fiber-linked optical atomic clocks," New J. Phys. 22(9), 093010 (2020).

[56] S. Kolkowitz, I. Pikovski, N. Langellier, M. D. Lukin, R. L. Walsworth, and J. Ye, "Gravitational wave detection with optical lattice atomic clocks," Phys. Rev. D 94(12), 124043 (2016).

[57] B. Hoffmann, "Noon-midnight red shift," Phys. Rev. 121(1), 337–342 (1961).

[58] C.-G. Qin, Y.-J. Tan, and C.-G. Shao, "The tidal clock effects of the lunisolar gravitational field and the Earth's tidal deformation," Astron. J. 160(6), 272 (2020).

[59] M. Takamoto, I. Ushijima, N. Ohmae, T. Yahagi, K. Kokado, H. Shinkai, and H. Katori, "Test of general relativity by a pair of transportable optical lattice clocks," Nat. Photonics 14, 411 (2020).

[60] P. Wolf and L. Blanchet, "Analysis of Sun/Moon gravitational redshift tests with the STE-QUEST space mission," Classical Quantum Gravity 33(3), 035012 (2016).

[61] B. Altschul et al., "Quantum tests of the Einstein equivalence principle with the STE-QUEST space mission," Adv. Space Res. 55(1), 501–524 (2015).

[62] A. Derevianko, K. Gibble, L. Hollberg, N. R. Newbury, C. Oates, M. S. Safronova, L. C. Sinclair, and N. Yu, "Fundamental physics with a state-of-the-art optical clock in space," Quantum Sci. Technol. 7(4), 044002 (2022).

[63] V. Schkolnik et al., "Optical atomic clock aboard an Earth-orbiting space station (OACESS): Enhancing searches for physics beyond the standard model in space," Quantum Sci. Technol. 8(1), 014003 (2022).

[64] E. D. Caldwell, L. C. Sinclair, N. R. Newbury, and J.-D. Deschenes, "The time-programmable frequency comb and its use in quantum-limited ranging," Nature 610, 667–673 (2022).

[65] D. R. Carlson et al., "Self-referenced frequency combs using high-efficiency silicon-nitride waveguides," Opt. Lett. 42(12), 2314–2317 (2017).

[66] D. D. Hickstein et al., "Ultrabroadband supercontinuum generation and frequency-comb stabilization using on-chip waveguides with both cubic and quadratic nonlinearities," Phys. Rev. Appl. 8(1), 014025 (2017).

[67] L. I. Gurvits, "Space VLBI: From first ideas to operational missions," Adv. Space Res. 65(2), 868–876 (2020).

[68] Z. Warren and R. Fields, "Optical crosslinks and satellite synchronization for GNSS, communications, and beyond," GPS Solutions 26(3), 64 (2022).

[69] V. L. Fish, M. Shea, and K. Akiyama, "Imaging black holes and jets with a VLBI array including multiple space-based telescopes," Adv. Space Res. 65(2), 821–830 (2020).

[70] The Event Horizon Telescope Collaboration et al., "First M87 event horizon telescope results. I. The shadow of the supermassive black hole," Astrophys. J. 875(1), L1 (2019).

[71] The Event Horizon Telescope Collaboration et al., "First M87 event horizon telescope results. II. Array and instrumentation," Astrophys. J. 875, L2 (2019).

[72] The Event Horizon Telescope Collaboration et al., "First M87 event horizon telescope results. III. Data processing and calibration," Astrophys. J. 875(1), L3 (2019).

[73] The Event Horizon Telescope Collaboration et al., "First M87 event horizon telescope results. IV. Imaging the central supermassive black hole," Astrophys. J. 875(1), L4 (2019).

[74] The Event Horizon Telescope Collaboration et al., "First M87 event horizon telescope results. V. Physical origin of the asymmetric ring," Astrophys. J. Lett. 875(1), L5 (2019).

[75] The Event Horizon Telescope Collaboration et al., "First M87 event horizon telescope results. VI. The shadow and mass of the central black hole," Astrophys. J. Lett. 875(1), L6 (2019).

[76] K. Akiyama et al., "First M87 event horizon telescope results. VII. Polarization of the ring," Astrophys. J. Lett. 910(1), L12 (2021).

[77] K. Akiyama et al., "First M87 event horizon telescope results. VIII. Magnetic field structure near the event horizon," Astrophys. J. Lett. 910(1), L13 (2021).

[78] T. M. Fortier et al., "Generation of ultrastable microwaves via optical frequency division," Nat. Photonics 5(7), 425–429 (2011).

[79] F. N. Baynes, F. Quinlan, T. M. Fortier, Q. Zhou, A. Beling, J. C. Campbell, and S. A. Diddams, "Attosecond timing in optical-to-electrical conversion," Optica 2(2), 141 (2015).

[80] T. Nakamura et al., "Coherent optical clock down-conversion for microwave frequencies with 10⁻¹⁸ instability," Science 368(6493), 889–892 (2020).

[81] A. E. E. Rogers and J. M. Moran, "Coherence limits for very-long-baseline interferometry," IEEE Trans. Instrum. Meas. IM-30(4), 283–286 (1981).

[82] R. Angélil, P. Saha, R. Bondarescu, P. Jetzer, A. Schärer, and A. Lundgren, "Spacecraft clocks and relativity: Prospects for future satellite missions," Phys. Rev. D 89(6), 064067 (2014).

[83] P. Delva et al., "Gravitational redshift test using eccentric galileo satellites," Phys. Rev. Lett. 121(23), 231101 (2018).

[84] E. M. Soop, Handbook of Geostationary Orbits (Microcosm, Inc., Torrance, CA, 1994).